Astronomy & Astrophysics manuscript no. main
May 8, 2025
©ESO 2025

Dust enrichment and growth in their earliest stages of protoplanetary disk formation

Eduard I. Vorobyov[1], Vardan G. Elbakyan[2], Alexandr Skliarevskii[3], Vitaly Akimkin[4], and Igor Kulikov[5]

[1] University of Vienna, Department of Astrophysics, Türkenschanzstrasse 17, 1180, Vienna, Austria; e-mail: eduard.vorobiev@univie.ac.at
[2] Fakultät für Physik, Universität Duisburg-Essen, Lotharstraße 1, D-47057 Duisburg, Germany
[3] Research Institute of Physics, Southern Federal University, Rostov-on-Don 344090, Russia
[4] Institute of Astronomy, Russian Academy of Sciences, Pyatnistkaya str., Moscow, 119017, Russia
[5] Institute of Computational Mathematics and Mathematical Geophysics SB RAS, Lavrentieva ave., 6, Novosibirsk, 630090 Russia

arXiv:2505.04233v1 [astro-ph.EP] 7 May 2025

ABSTRACT

Aims. Dust enrichment and growth during the initial stages of protoplanetary disk formation were numerically investigated. A particular objective was to determine the effects of various growth barriers, which were mimicked by setting a series of upper permissible limits on maximum dust sizes.
Methods. We used the ngFEOSAD code to simulate the three-dimensional dynamics of gas and dust in the polytropic approximation starting from the gravitational collapse of a slowly rotating Bonnor-Ebert sphere to ≈ 12 kyr after the first hydrostatic core and disk formation.
Results. We found that dust growth starts in the contracting cloud in the evolution stage that precedes disk formation and the disk begins to form in an environment that is already enriched in grown dust. The efficiency of dust growth in the disk is limited by dust growth barriers. For dust grains with maximum size < 100 μm these are likely electrostatic or bouncing barriers, and for larger grains the fragmentation and drift barriers play the major role. The disk midplane becomes quickly enriched with dust, while the vertically integrated distribution of dust shows notable local variations around the canonical 1:100 dust-to-gas mass ratio. These positive and negative deviations are likely caused by local hydrodynamic flows, since the globally integrated dust-to-gas ratio deviates negligibly from the initial 1:100 value. We note that care should be taken when considering models with a fixed dust size, as it may attain a profound negative radial gradient already in the very early stages of disk formation. Models with a constant Stokes number may be preferable in this context.
Conclusions. The early dust enrichment and growth may facilitate planet formation as suggested by observations of protoplanetary disk substructures.

Key words. Protoplanetary disks – Hydrodynamics – Stars: formation

1. Introduction

Dust enrichment and growth during the evolution of a protoplanetary disk are key to planet formation. When these crucial steps towards planet formation occur is not yet fully understood. Dust in the interstellar medium is of a sub-μm size (Mathis et al. 1977), while protoplanetary disks in the early T Tauri stage may already host protoplanets as implied by the presence of deep gaps in the gas and dust radial density distributions (ALMA Partnership et al. 2015; van der Marel et al. 2019). This requires dust growth by many orders of magnitude over a time period of a few hundred thousand years, starting from gravitational contraction of a prestellar cloud and ending with cloud dissipation and accretion onto a young stellar object.

There is growing evidence that the initial stages of dust enrichment above the interstellar value of 1:100 may already occur in the stage that precedes disk formation. This stage is characterized by the gravitational contraction of a prestellar cloud followed by the formation of the first hydrostatic core (hereafter, FHSC) in the parlance of Larson (Larson 1985). Observations of young stellar objects suggest the presence of dust grains with a size up to 100 μm in the protostellar envelopes (Galametz et al. 2019; Valdivia et al. 2019). The prevailing explanation for the presence of such large grains are disk winds, which can lift grains that have already experienced some growth in the disk to hundreds of astronomical units above the disk midplane (Tsukamoto et al. 2021; Koga & Machida 2023; Morbidelli et al. 2024). Numerical modeling of dust growth in protostellar envelopes seems to support this scenario, suggesting that dust may grow to a few microns only (Silsbee et al. 2022).

However, limitations of current grain growth models permit that some microphysical processes, which are not yet fully understood, may still allow dust to grow in-situ to > 1.0 μm-sized grains faster than expected (Morbidelli et al. 2024). For instance, (Bate 2022) found that dust growth to ≤ 100 μm can occur in the inner several hundreds of astronomical units, and in particular in the FHSC. The latter object is not only a transitional structure on the way to the protostar, which begins to form when the temperature in the FHSC interior reaches a threshold value for molecular hydrogen dissociation (Masunaga & Inutsuka

2000a), but may also be a transitional phase to the protoplanetary disk, which may form around the FHSC even earlier than around the protostar itself (Inutsuka 2012; Tomida et al. 2015). Dust grains may dynamically decouple from gas already in the protostellar envelope and the ensuing differential collapse of dust with respect to the gas may enrich the protoplanetary disk right from the instance of its formation (Tsukamoto et al. 2017; Cridland et al. 2022).

Fast dust growth in the earliest stages of disk formation was reported in several recent studies. For instance, Marchand et al. (2023) found that, starting from sub-micron radii, grain sizes reach more than 100 μm in an inner protoplanetary disk that is only one thousand years old, see also Bate (2022) and Vorobyov et al. (2024). Further dust growth and enrichment in the protoplanetary disk stage can, however, be hindered by dust growth barriers caused by electrostatic repulsion, bouncing, fragmentation, and drift (Birnstiel 2024). Considering self-consistently these barriers in dust growth models coupled to disk hydrodynamics simulations is a difficult task. It requires calculating the ionization balance and dust charging, the internal structure of dust grains, and their dynamics with respect to gas. Perhaps, the fragmentation barrier is the easiest to consider by choosing a certain value of the dust fragmentation velocity, which sets the upper dust size in the so-called fragmentation limited regime. However, a wide uncertainty in the value of the fragmentation velocity (Wada et al. 2009; Gundlach & Blum 2015; Blum 2018) results in a wide variation of the dust disk properties depending on the actual value of this parameter (Vorobyov et al. 2023a). The problem of dust growth and drift in hydrodynamics models can be further simplified by considering dust dynamics for a range of fixed dust grain sizes (or fixed Stokes number) (e.g., Rice et al. 2004; Rowther et al. 2024) or in the steady-state terminal velocity approximation (e.g., Lebreuilly et al. 2020). It is, however, not clear when the assumptions of fixed dust size or Stokes number can be used.

Considering the complicated nature of dust growth barriers, it makes sense to tackle the problem of the maximum achievable dust size using a simplified approach. In this work, we make a series of controlled numerical experiments of dust dynamics and growth in the pre- and immediate post-disk formation phases using the three-dimensional ngFEOSAD code. We let dust grow via mutual collisions but artificially limit its maximum size by a certain cap value, which is chosen in the 10 μm - 100 cm limits. We examine the results to draw conclusions that can be useful for inferring the relative importance of various growth barriers, and also for the applicability of focused simulations of dust dynamics with fixed dust size or Stokes number. The initial sources of dust enhancement are also identified and discussed.

The paper is organized as follows. Sect. 2 describes the hydrodynamics model employed to simulate the earliest stages of disk formation. Main results are presented in Sect. 3. Model caveats are described in Sect. 4 and main conclusions are summarized in Sect. 5.

2. Model description

The simulations were performed using the the Formation and Evolution Of Stars and Disks on nested grids (ngFEOSAD) code. The pertinent equations and the solution methods were thoroughly described in (Vorobyov et al. 2024). Here, we briefly review the main concepts and equations, and refer the reader to the aforementioned work for more details. With ngFEOSAD we compute the co-evolution of gas and dust in the initial stages of protoplanetary disk formation, starting from the gravitational collapse of a slowly rotating prestellar Bonnor-Ebert sphere in a fully three-dimensional manner. We adopt a barotropic equation of state, which includes the initial isothermal collapse stage followed by the FHSC and disk formation stages, up to the hydrogen dissociation stage, at which the protostar begins to form. We note that we terminate our simulations before the instance of protostar formation because this process cannot be fully resolved in our three-dimensional simulations with limited spatial resolution (≥ 0.14 au in the central regions). Furthermore, we are interested in the processes occurring in the forming disk rather than in the protostellar interiors, for which numerical models with lower dimensionality are better suited (Bhandare et al. 2020). We also do not introduce the sink cell as the results may be sensitive to the details of the sink cell implementation (Machida et al. 2014; Vorobyov et al. 2019; Hennebelle et al. 2020), which requires a careful consideration and is currently under development.

2.1. Gas component

The dynamics of gas is followed by solving the equations of continuity and momentum

$$\frac{\partial \rho_{\rm g}}{\partial t} + \nabla \cdot (\rho_{\rm g} \boldsymbol{v}) = 0, \tag{1}$$

$$\frac{\partial}{\partial t}(\rho_{\rm g} \boldsymbol{v}) + \nabla \cdot (\rho_{\rm g} \boldsymbol{v} \otimes \boldsymbol{v} + \mathbb{I} P) = -\rho_{\rm g} \nabla \Phi - \rho_{\rm d,gr} \boldsymbol{f}, \tag{2}$$

where $\rho_{\rm g}$ is the volume gas density, Φ the gravitational potential, $\boldsymbol{v}$ the gas velocity, P the gas pressure, $\mathbb{I}$ the unit tensor, and $\boldsymbol{f}$ the friction force per unit dust mass between gas and dust.

We used the following barotropic equation for the closure relation between gas pressure and density

$$P_k = c_{\rm s,0}^2 \, \rho_{\rm g}^{\gamma_k} \prod_{i=1}^{k-1} \rho_{{\rm c},i}^{\gamma_i - \gamma_{i+1}}, \;\; \text{for} \;\; \rho_{{\rm c},k-1} \leq \rho_{\rm g} < \rho_{{\rm c},k}\,, \tag{3}$$

where $c_{\rm s,0} = \sqrt{\mathcal{R} T_{\rm in}/\mu}$ is the initial isothermal sound speed, $T_{\rm in}$ the initial gas temperature, $\mathcal{R}$ the universal gas constant, and $\mu = 2.33$ the mean molecular weight. The values of the indices i and k distinguish the four individual components of the piecewise form shown in Table 1. The first component corresponds to the initial isothermal stage of cloud core collapse, while the other three components account for the postcollapse nonisothermal evolution with various ratios of the specific heat $\gamma_{i(k)}$ (Masunaga & Inutsuka 2000a; Machida & Nakamura 2015). We note that when $k = 1$ the product term is unity by definition, and the pressure reduces to $P_1 = c_{\rm s}^2 \rho_{\rm g}^{\gamma_1}$. The gas pressure P in Equation (2) is set equal to P_k, where the index k is defined by the condition that $\rho_{\rm g}$ falls in between the corresponding critical densities, $\rho_{{\rm c},k-1} \leq \rho_{\rm g} < \rho_{{\rm c},k}$.

Table 1. Parameters of the barotropic relation.

k	$\gamma_{i(k)}$	$n_{\mathrm{c},i(k)}$ (cm^{-3})
1	1.00	$5{\times}10^{10}$
2	1.6667	$2.5{\times}10^{12}$
3	1.4	1.5×10^{15}
4	1.1	...

Notes. The coefficients γ_i and $n_{\mathrm{c},i}$ were taken from Machida & Nakamura (2015). The number density $n_{\mathrm{c},i}$ is related to the volume density $\rho_{\mathrm{c},i}$ as $\rho_{\mathrm{c},i} = \mu m_{\mathrm{H}} n_{\mathrm{c},i}$, where m_{H} is the mass of hydrogen atom.

2.2. Dust component

In this work, dust is considered as a pressureless fluid (see Appendix A) with two populations: small dust that is dynamically linked to gas and grown dust that can dynamically decouple from gas. The pertinent dynamics equations are

$$\frac{\partial \rho_{\mathrm{d,sm}}}{\partial t} + \nabla\cdot(\rho_{\mathrm{d,sm}}\boldsymbol{v}) = -S(a_{\max}), \tag{4}$$

$$\frac{\partial \rho_{\mathrm{d,gr}}}{\partial t} + \nabla\cdot(\rho_{\mathrm{d,gr}}\,\boldsymbol{u}) = S(a_{\max}), \tag{5}$$

$$\begin{aligned}\frac{\partial}{\partial t}(\rho_{\mathrm{d,gr}}\,\boldsymbol{u}) + \nabla\cdot(\rho_{\mathrm{d,gr}}\,\boldsymbol{u}\otimes\boldsymbol{u}) &= -\rho_{\mathrm{d,gr}}\,\nabla\Phi + \rho_{\mathrm{d,gr}}\,\boldsymbol{f}\\ &+ S(a_{\max})\,\boldsymbol{v},\end{aligned} \tag{6}$$

where $\rho_{\mathrm{d,sm}}$ and $\rho_{\mathrm{d,gr}}$ are the volume densities of small and grown dust, respectively, $\boldsymbol{u}$ the velocity of grown dust, and $S(a_{\max})$ the conversion rate between small and grown dust populations.

This two-component dust model was originally developed in Vorobyov et al. (2018) with modifications to account for the back-reaction on gas in Stoyanovskaya et al. (2018). We define small dust as grains with a size between $a_{\min} = 5\times10^{-3}$ μm and $a_* = 1$ μm and grown dust as aggregates ranging in size from a_* to $a_{\max}$. The value of a_* that separates small dust from grown dust is chosen so as to make grown dust dynamically decoupled and small dust dynamically coupled to gas in the protoplanetary disk environment Vorobyov et al. (2022, see Appendix D). However, in the collapsing cloud core the dust-to-gas decoupling may occur even at smaller than $a_* = 1.0$ μm dust sizes owing to lower gas densities. The dependence of our results on the choice of a_* will be considered in a follow-up paper. Small dust dynamics in the terminal velocity approximation (e.g., Laibe & Price 2014; Lin & Youdin 2017) is another planned improvement for our model.

Initially, the total dust mass budget in a collapsing prestellar cloud is partitioned as 70%:30% between the small and grown dust populations (see Sect. 2.7). The former can further grow and turn into grown dust as the collapse proceeds, and the disk forms and evolves. It is assumed that dust in both populations is distributed over size according to a simple power law:

$$N(a) = C\cdot a^{-\mathrm{p}}, \tag{7}$$

where C is a normalization constant and $\mathrm{p} = 3.5$. We note that the power index p is kept constant in this study, but it may also vary if the form of this variation is known from more sophisticated dust growth models.

2.3. Dust growth model

The maximum value of the dust size $a_{\max}$ is calculated using a simple monodisperse dust growth model and can be variable in space and time. We use the following equation describing the time evolution of $a_{\max}$

$$\frac{\partial a_{\max}}{\partial t} + (\boldsymbol{u}\cdot\nabla)a_{\max} = \mathcal{D}, \tag{8}$$

where the rate of dust growth due to collisions and coagulation is computed using a monodisperse model (Birnstiel et al. 2012)

$$\mathcal{D} = \frac{\rho_{\mathrm{d}}\,u_{\mathrm{rel}}}{\rho_{\mathrm{s}}}. \tag{9}$$

This rate includes the total volume density of dust $\rho_{\mathrm{d}} = \rho_{\mathrm{d.sm}} + \rho_{\mathrm{d,gr}}$, dust material density ρ_{s}, and relative velocity of grain-to-grain collisions defined as $u_{\mathrm{rel}} = (u_{\mathrm{br}}^2 + u_{\mathrm{turb}}^2)^{1/2}$, where u_{br} and u_{turb} account for the Brownian and turbulence-induced local motion of dust grains, respectively. In particular, u_{turb} has the biggest contribution to dust growth in our model and is expressed as (Ormel & Cuzzi 2007)

$$u_{\mathrm{turb}} = \sqrt{\frac{3\alpha}{\mathrm{St}+\mathrm{St}^{-1}}}\,c_{\mathrm{s}}, \tag{10}$$

where c_{s} is the adiabatic speed of sound, α is the parameter describing the strength of turbulence in the disk, and St is the Stokes number defined as $\mathrm{St} = t_{\mathrm{stop}}\Omega_{\mathrm{K}}$. Here, Ω_{K} is the Keplerian angular velocity and t_{stop} is the stopping time. The α parameter describes the level of turbulence in the disk and is set to 10^{-3}, implying low turbulence, which is consistent with observations (Rosotti 2023). Determining Ω_K on the fly during the simulations turned out nontrivial. We tried to use the local angular velocity as a proxy of Ω_{K} but that worked poorly in disks perturbed by spiral density waves and mass infall from the envelope. As in our previous work (Vorobyov et al. 2024), we set Ω_K equal to that of a 0.05 $M_\odot$ central object, which is roughly the upper mass of the FHSC (Tomida et al. 2010). Considering that we limit our runs to the very early stages of star and disk formation, this should introduce only small errors to u_{turb}.

As the maximum size of dust grains $a_{\max}$ begins to increase according to the adopted dust growth model, part of the small dust population is converted to grown dust. This process is described by the conversion rate $S(a_{\max})$, which can be expressed as

$$S(a_{\max}) = \frac{1}{\Delta t}\frac{\rho^n_{\mathrm{d,sm}}\int_{a_*}^{a^{\mathrm{n+1}}_{\max}} a^{3-\mathrm{p}}da - \rho^n_{\mathrm{d,gr}}\int_{a_{\min}}^{a_*} a^{3-\mathrm{p}}da}{\int_{a_{\min}}^{a^{\mathrm{n+1}}_{\max}} a^{3-\mathrm{p}}da}, \tag{11}$$

which is derived assuming the conservation of dust mass and continuous dust size distribution across a_* (see Eq. 7). Here, Δt hydrodynamic time step and the indices n and $n+1$ denote the current and next hydrodynamic steps of integration, respectively. The detailed derivation can be found in Molyarova et al. (2021) and Vorobyov et al. (2022).

2.4. Dust growth barriers

Dust growth in a protoplanetary disk is hindered by the so-called barriers, among which are the bouncing barrier, fragmentation barrier, radial drift barrier, and electrostatic barrier (Okuzumi 2009; Zsom et al. 2010; Wada et al. 2011; Okuzumi et al. 2011a; Windmark et al. 2012; Birnstiel et al. 2016; Akimkin et al. 2020, 2023a). Each barrier depends sensitively on the local physical conditions in the disk and on the dust properties. For instance, the fragmentation barrier increases as the fragmentation velocity squared. This latter quantity is currently poorly constrained and may vary from 0.5 m s^{-1} to tens of meters per second (Blum & Wurm 2008; Wada et al. 2009; Gundlach & Blum 2015). The electrostatic barrier depends on the relative number of dust grains to that of charge carriers (electrons and ions), and also on the temperature and the degree of turbulence in the disk (Akimkin 2015). The bouncing barrier depends on the relative velocity of colliding dust particles and their structure, namely on the filling factor (Wada et al. 2011).

Among these barriers, only the radial drift barrier can be account for in our simulations self-consistently because we solve full equations of gas and dust dynamics including their mutual friction (see below). But considering self-consistently the other barriers is problematic. Therefore, we took a simplified approach and imposed a maximum dust size $a_{\max}^{\rm cap}$, which caps dust growth via mutual collisions. More specifically, when $a_{\max}$ defined by Equation (8) exceeds $a_{\max}^{\rm cap}$, the growth rate $\mathcal{D}$ described by Equation (9) is set equal to zero and $a_{\max}$ is set equal to $a_{\max}^{\rm cap}$.

For $a_{\max}^{\rm cap}$, we considered six different values 10 μm, 100 μm, 1.0 mm, 1.0 cm, 10 cm, and 100 cm, which are constants of time and space. The lowest value of $a_{\max}^{\rm cap} = 10$ μm can be considered as the threshold imposed by the electrostatic barrier, which usually suspends dust growth at several μm until the barrier is broken, firstly in the outer cold disk regions (Okuzumi 2009; Zsom et al. 2010; Okuzumi et al. 2011b; Akimkin 2015; Steinpilz et al. 2020; Akimkin et al. 2023b). The largest value of $a_{\max}^{\rm cap} = 100$ cm may represent the fragmentation barrier with the highest fragmentation velocity of several tens of meters per second for compact ice dust aggregates (Wada et al. 2009). The intermediate values of $a_{\max}^{\rm cap}$ can be regarded as those representing a combination of fragmentation and bouncing barriers for a possible spectrum of fragmentation velocities and bouncing efficiency.

2.5. Drag force

The drag force between dust and gas in our work is calculated as

$$\boldsymbol{f} = \frac{\boldsymbol{v} - \boldsymbol{u}}{t_{\rm stop}}, \tag{12}$$

where the stopping time $t_{\rm stop}$ is expressed as

$$t_{\rm stop} = \frac{a\,\rho_{\rm s}}{\rho_{\rm g} v_{\rm th}}. \tag{13}$$

Here, $v_{\rm th}$ is the mean thermal velocity of gas and $\rho_{\rm s} = 3.0$ g cm^{-3} is the material density of dust grains. Since grown dust in our model has a spectrum of sizes from a_* to $a_{\max}$, the size of dust grains a in Equation (13) should be weighted over this spectrum. However, the span between a_* to $a_{\max}$ may become as large as several orders of magnitude during the disk evolution and the average size of dust grains $\sqrt{a_* a_{\max}}$ becomes much smaller than $a_{\max}$. In this work, we are interested in the dynamics of dust grains that are the main dust mass carriers. For the chosen slope $p = 3.5$, large grains near $a_{\max}$ mostly determine the dust mass (Birnstiel et al. 2016). Therefore, we use the maximum size of dust grains $a_{\max}$ when calculating the values of $t_{\rm stop}$. We also note that Equation 13 assumes that dust is in the Epstein drag regime, where the mean free path of hydrogen molecules is much larger than the size of dust grains. This condition breaks, for instance, in the Stokes regime, and the stopping time has to be modified accordingly (see, e.g. Vorobyov et al. 2023a; Birnstiel 2024). As Figure 3 below demonstrates, the Stokes regime occurs only for models with $a_{\max}^{\rm cap} \geq 1.0$ cm and only in the inner several astronomical units occupied by the FHSC. Since our study is mainly focused on dust dynamics and growth in the disk and collapsing envelope, the Epstein drag regime is justified.

2.6. Distinguishing the disk from the infalling envelope

In our numerical simulations, we often distinguish the disk from the infalling envelope for the convenience of the analysis. To do that, we adopted the disk tracking conditions outlined in Joos et al. (2012). In particular, we use the following criteria to determine if a particular computational cell belongs to the disk:

- the gas rotational velocity must be faster than twice the radial infall velocity, $v_\phi > 2v_{\rm r}$,
- the gas rotational velocity must be faster than twice the vertical infall velocity, $v_\phi > 2v_{\rm z}$,
- gas must not be thermally supported, $\frac{\rho_{\rm g} v_\phi^2}{2} > 2P$,
- the gas number density must be higher than 10^{10} cm^{-3}.

Here, $v_{\rm z}$, $v_{\rm r}$, and v_ϕ are the components of gas velocity in the cylindrical coordinates, $\rho_{\rm g}$ the volume density of gas, and P the gas pressure. If any of the first three conditions fail, a particular grid cell is not qualified as belonging to the disk. The forth condition must always be fulfilled. We note that we have increased the threshold for the gas number density to 10^{10} cm^{-3} as compared to 10^9 in Joos et al. (2012) because the former value better describes the disk in our models.

2.7. Initial and boundary conditions

For the initial cloud core configuration, we construct a Bonnor-Ebert sphere with the central density 3×10^4 cm^{-3}. The ratio of the central density to that at the outer edge of the sphere, a quantity that determines the shape of the sphere and its stability to gravitational collapse, is set equal to 15, making the sphere marginally unstable. The initial temperature is set equal to 10 K. The ratio of rotational to gravitational energy is $\beta = 0.5\%$ and the ratio of thermal to gravitational energy is 70%.

The initial dust size distribution spans a range between 5×10^{-3} μm and 2.0 μm, as suggested by the MRN distribution in the interstellar clouds (Mathis et al. 1977). The division between small and grown dust grains at $a_* = 1.0$ μm is, however, arbitrary. This value was initially motivated by long drift timescales of dust with size ≤ 1.0 μm in the midplane of a protoplanetary disk (Vorobyov et al. 2022), allowing us to neglect the dynamics of small dust. However, this may not be the case in a collapsing cloud core, as is shown further in Sect. 3, and the effects of smaller a_* will be considered in a follow-up study. For the adopted slope of the dust size distribution $p = 3.5$, about 70% of the total dust mass budget is in the form of small dust grains, while the rest is in the form of grown dust. The initial total dust-to-gas mass ratio is 0.01.

The cloud is initially submerged into an external medium with pressure that is chosen so as to hold the Bonnor-Ebert sphere in marginal equilibrium. To initiate the collapse, we give the cloud an initial positive gas and dust density perturbation of 30%, namely, we increase the corresponding densities by 30%. The resulting mass of the unstable cloud core is $M_{\rm cl} = 0.89$ $M_\odot$ and its radius is $R_{\rm cl} = 3.9 \times 10^{-2}$ pc.

2.8. Numerical solution method

To solve the equation of hydrodynamics for the gas component, we employ the Godunov method with the HLLC (Harten–Lax–van Leer contact) Riemann solver (Toro 2019). The equations for the grown dust component are also solved by the Godunov method, similar to that used to solve the hydrodynamic equations, but with the help of a one-wave HLL Riemann solver owing to the specifics of the pressureless dust fluid. The gravity and friction forces are considered separately after the Godunov step. The gravitational potential is found using the fast Fourier transform and the convolution theorem as described for the case of regular grids in Binney et al. (1987), with modifications for nested meshes as described in Vorobyov et al. (2023b). The method is globally second-order accurate, except for the grid interfaces where the first-order interpolation of the boundary values is applied. The update of the gas and dust velocities due to the friction force $\boldsymbol{f}$ between dust and gas is computed using an analytic solution, which can be obtained under the assumption of constant values of $t_{\rm stop}$ and dust-to-gas ratio in a given cell during a hydrodynamical time step (Lorén-Aguilar & Bate 2015; Stoyanovskaya et al. 2018). The time step is calculated using the Courant-Friedrichs-Lewy condition with the Courant number set equal to 0.25. A detailed description of the solution procedure and the pertinent tests were provided in Vorobyov et al. (2024).

We employed Coarray Fortran for the distributed memory parallelism, which is much simpler in coding than the usual message-passing interface (MPI), while being only slightly inferior to the MPI in terms of the speed (McKevitt et al. 2024). ngFEOSAD is fast and environmentally friendly. For this work we used 12 nested levels with 64 cells in each coordinate direction, thus amounting to approximately 3.15 million grid cells in total and having a minimum spatial resolution of ≈ 0.1 au in the inner several astronomical units. The typical run-time was 20 days on AMD EPYC 7713 processors with four nodes, amounting to 192 cores in total. This corresponds roughly to 92,000 core-hours.

3. Main results

Once the initial Bonnor-Ebert sphere is given a positive density perturbation, it begins to contract under the force of its own gravity while gradually spinning up. The FHSC begins to form in the vicinity of the coordinate center at ≈ 193 kyr after the onset of the simulations, as indicated by positive deviations of the gas temperature in this region from the initial isothermal value of 10 K. The temperature at the center of the FHSC by the end of numerical simulations (204.5 kyr) reaches ≈ 1800 K, just marginally below the threshold temperature for molecular hydrogen dissociation, the process that leads to the collapse of the FHSC and the formation of the protostar (Masunaga & Inutsuka 2000b). We note that our limited numerical resolution does not allow us to follow protostar formation. Furthermore, the transition from the FHSC to protostar may occur somewhat earlier than predicted in our model because we do not fully resolve the inner regions and the gas temperature is washed out over the inner 0.1 au. Radiation transfer simulations are needed to better follow the evolution of gas temperature in the FHSC (Tomida et al. 2010; Bhandare et al. 2018; Ahmad et al. 2023), a module that is currently under development for ngFEOSAD.

3.1. General disk evolution analysis

Figure 1 presents the time evolution of the gas density $\rho_{\rm g}$ in the midplane ($z = 0$) for all six models with different allowed maximum dust sizes $a_{\rm max}^{\rm cap}$. The disk grows around the FHSC as material with increasingly higher angular momentum is accreted from the infalling envelope. In these images, the disk can be distinguished from the infalling envelope not only by a higher density, but also as the regions characterized a profound nonaxisymmetric pattern with a dominant two-armed spiral. These "pre-stellar" disks were also observed to be gravitationally unstable in other three-dimensional hydrodynamics simulations (e.g. Inutsuka 2012; Bate 2022). The gravitational instability in such a young disk is sustained by infall from the envelope. This process was first reported in two-dimensional thin-disk simulations by Vorobyov & Basu (2005), further studied in detail in semi-analytic models of Kratter et al. (2008), and was also detected in HH 111 VLA (Lee et al. 2020). Since the gravitational instability is a stochastic process, small variations in gas dynamics in the disk formation stage caused by friction of gas with dust of different size lead to different shapes of the spiral pattern, but overall the gas disk evolution is similar in all considered models.

Figure 2 displays the radial profiles of several disk characteristics in the midplane ($z = 0$) at $t = 12$ kyr after the disk formation instance. The data belonging to the disk according to the adopted disk tracking mechanism (see Sect. 2.6) are plotted, while the infalling envelope is excluded from the analysis. The radial profiles of gas volume density, grown dust density, and temperature show small variations from model to model but are rather similar in the shape. The formation of the FHSC is most evident in the radial temperature profiles showing a plateau with a nearly constant temperature of 1800 K that extends up to 1.0 au. A similar but less expressed plateau can be seen

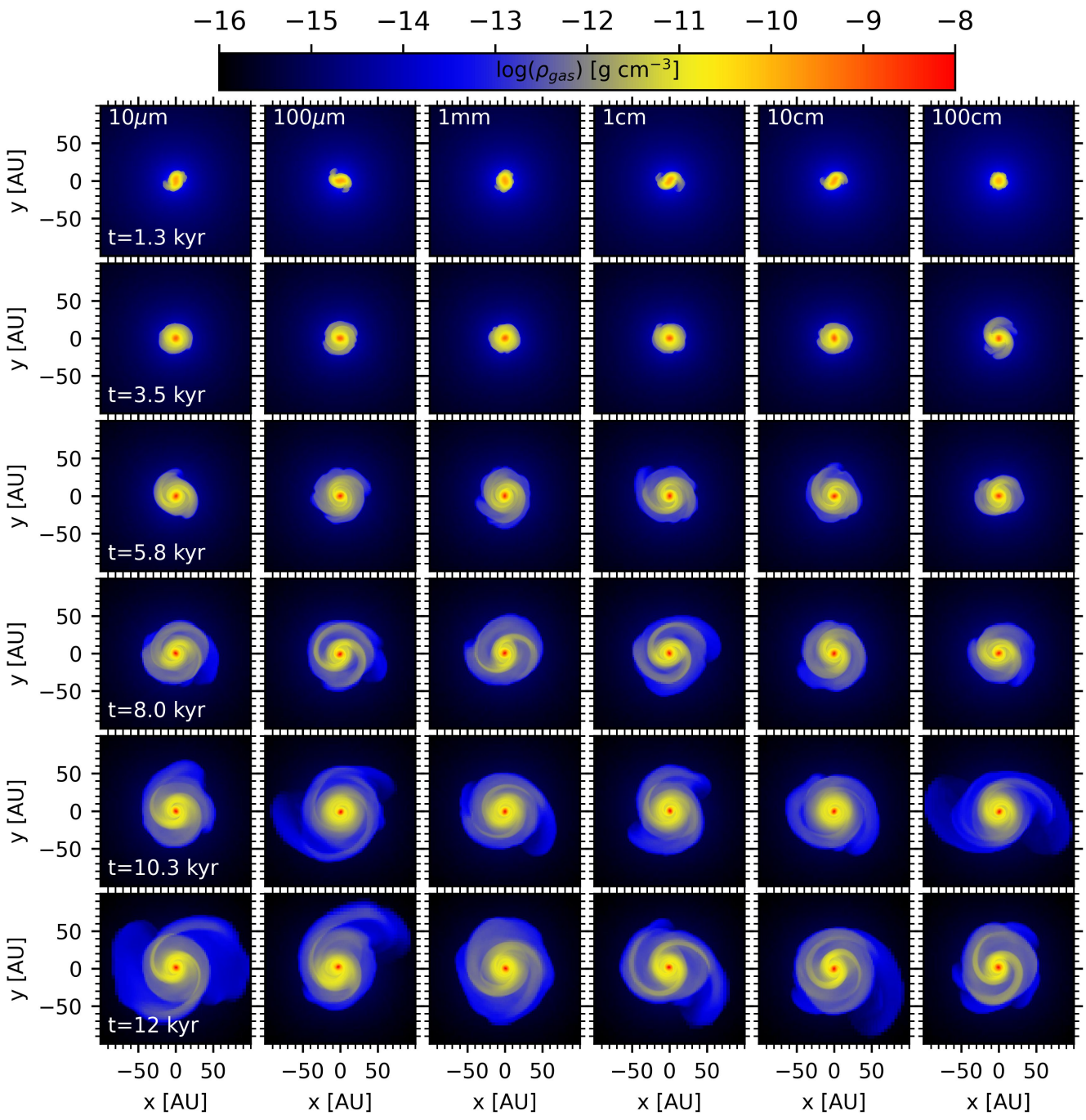


Fig. 1. Time evolution of the gas volume density in the disk midplane in all six models considered. Columns from left to right correspond to models with the maximum allowed dust size of 10 μm, 100 μm, 1.0 mm, 1.0 cm, 10 cm, and 100 cm, respectively. Shown is the inner spatial region of 200 × 200 au^2 in size. The time is counted from the disk formation instance.

in the gas density distribution. The plateau in the grown dust density is least expressed, in particular, for large $a_{\rm max}^{\rm cap}$, which is likely caused by inward radial drift. We note that the small dust density is systematically smaller across the entire disk extent for models with higher $a_{\rm max}^{\rm cap}$, which reflects efficient conversion of small dust into grown dust during the process of dust growth. We can conclude that the fragmentation barrier may have a notable effect on dust in the early stage of disk evolution. Gas dynamics may also be indirectly affected via the varying ionization fraction, which depends on the surface area of dust grains, and via the varying dust opacity, which is sensitive to the minimum and maximum dust sizes.

3.2. Radial distributions of maximum dust size and Stokes number

Orange symbols in Figure 3 display the maximum dust size in the disk midplane for the six models with different $a_{\rm max}^{\rm cap}$. It is useful to compare our model data with what would be expected from the fragmentation-limited dust growth models. The thick blue curves show the maximum size that

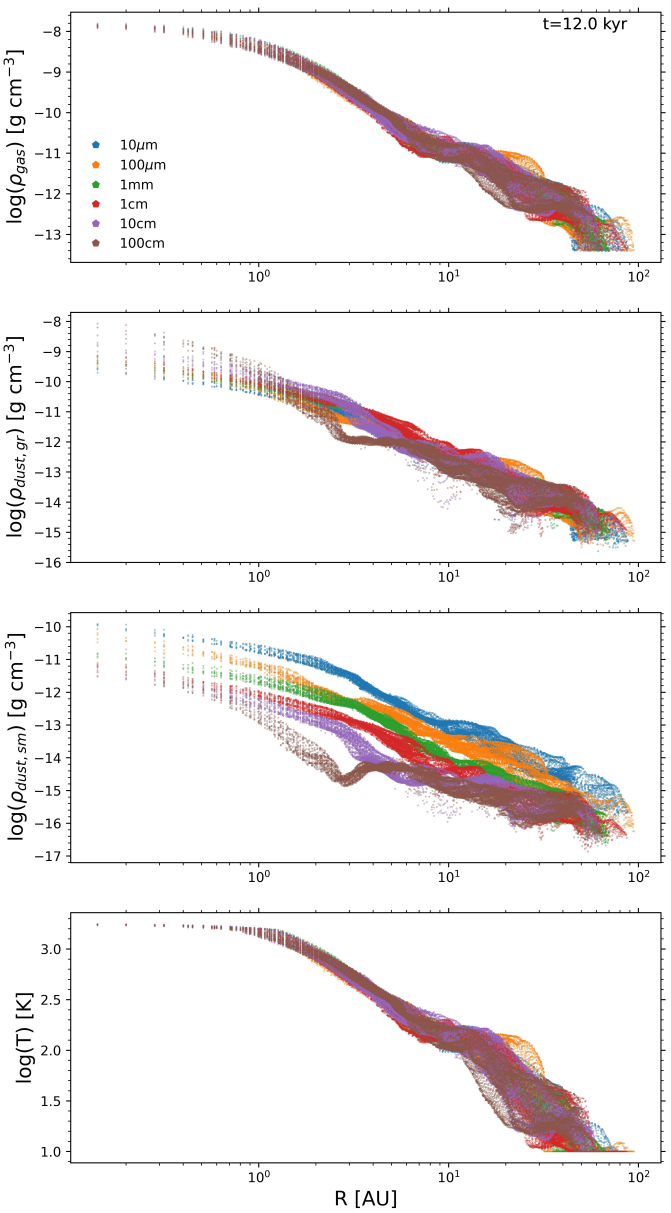


Fig. 2. Radial dependence of disk midplane characteristics for all six models. Shown are (from top to bottom): the gas volume density, the grown dust volume density, the small dust volume density, and temperature.

dust grains would attain in our models if their collisional growth were limited by fragmentation with the values of fragmentation velocity $u_{\rm frag}$ = 0.5 m s^{-1}, 10 m s^{-1}, and 50 m s^{-1} (Wada et al. 2009; Okuzumi et al. 2016). These curves essentially represent the fragmentation barriers for the chosen fragmentation velocities, where the barriers are calculated similarly to the definition given in Birnstiel et al. (2016) but considering the three-dimension nature of our modeling as (volume densities instead of column densities)

$$a_{\rm frag} = \frac{\rho_{\rm g} u_{\rm frag}^2}{3\alpha\rho_{\rm s} v_{\rm th}\Omega_{\rm K}}. \quad (14)$$

where $\Omega_{\rm K}$ is the Keplerian angular velocity. The thin dotted curves show the dust size that particles would have in our models if they were characterized by a fixed Stokes number: from St = 10^{-3} through 10^{-2} and to 10^{-1}. Both blue and dotted curves were obtained by first calculating the corresponding values in the entire disk and then taking an arithmetic average along the azimuth at each radial distance. Small-scale variations are caused by nonaxisymmetries in our model disk, an effect that is absent in a similar figure 4 derived for an axisymmetric disk model in Drążkowska et al. (2023).

Several conclusions can be drawn from Figure 3 when comparing the radial distributions of $a_{\rm max}$ in our models with the considered fragmentation barriers $a_{\rm frag}$ and the lines of constant St. First, for $a_{\rm max}^{\rm cap}$=10 μm the fragmentation barrier is not reached, even for the lowest considered fragmentation velocity of $u_{\rm frag}$ = 0.5 m s^{-1}. If dust particles of such a small size are inferred from observation of young disks, then their growth should be limited by barriers other than that of collisional fragmentation, or the fragmentation velocity is still lower than 0.5 m s^{-1}. The Stokes numbers of these grains are much smaller than 10^{-3}, implying that radial drift is insignificant in this case (see also discussion to Figure 4 below).

For $a_{\rm max}^{\rm cap}$=100 μm the fragmentation barrier for the lowest considered fragmentation velocity of $u_{\rm frag}$ = 0.5 m s^{-1} is marginally reached in the disk region starting from 5-6 au and up to the disk outer edge. Detection of dust particles of 100 μm may therefore imply a quite low fragmentation velocity of 0.5 m s^{-1}. The dust particles approach St = 10^{-3} in the outermost disk regions, but the bulk of the disk midplane is still below this value. In both cases, $a_{\rm max}^{\rm cap}$=10 μm and $a_{\rm max}^{\rm cap}$=100 μm, the dust growth is saturated at our imposed upper limit and the drift barrier is inefficient at setting the maximum dust size.

For $a_{\rm max}^{\rm cap}$=1.0 mm and 1.0 cm, the maximum dust sizes lie within those defined by the fragmentation barriers with $u_{\rm frag}$ = 0.5 m s^{-1} and $u_{\rm frag}$ = 10 m s^{-1}. In both models a region appears where dust growth is not saturated ($a_{\rm max}$ is smaller than the corresponding $a_{\rm max}^{\rm cap}$), implying that radial drift now becomes efficient and dust grains cannot reach our imposed upper limits on the maximum dust size. Indeed, the Stokes numbers are now above 10^{-3}, reinforcing our conclusion that radial dust drift is no more negligible. Interestingly, the $a_{\rm max}^{\rm cap}$=1.0 cm model can be described by a slowly varying St, ranging between 10^{-3} and 10^{-2}, in the disk regions from 10 au and further out.

For $a_{\rm max}^{\rm cap}$=10 and 100 cm, dust growth saturates only in the inner several astronomical unit, while the drift dominated region extends further inwards and almost reaches the FHSC for the latter model. The maximum dust sizes lie mostly below those imposed by the fragmentation barrier with $u_{\rm frag}$ = 10 m s^{-1}, with an exception of the innermost regions where an even higher $u_{\rm frag}$ is needed to account for the values of $a_{\rm max}$. The trend of $a_{\rm max}$ being arranged along the lines of constant Stokes number (close to 10^{-2}) becomes even more pronounced for these two models.

If the electrostatic barrier is passed (perhaps, already in the collapse stage), then dust can grow to submm-, mm-, or even cm-sized grains in the disk already in the evolution stage preceding the formation of the protostar via the collapse of the FHSC, depending on the details of dust fragmentation and drift processes. Such a fast dust growth was also noticed in previous studies of the disk formation stages (e.g., Vorobyov et al. 2018; Bate 2022). Furthermore, the existence of large grains seems to be confirmed in observations of the inner disk regions in systems with luminos-

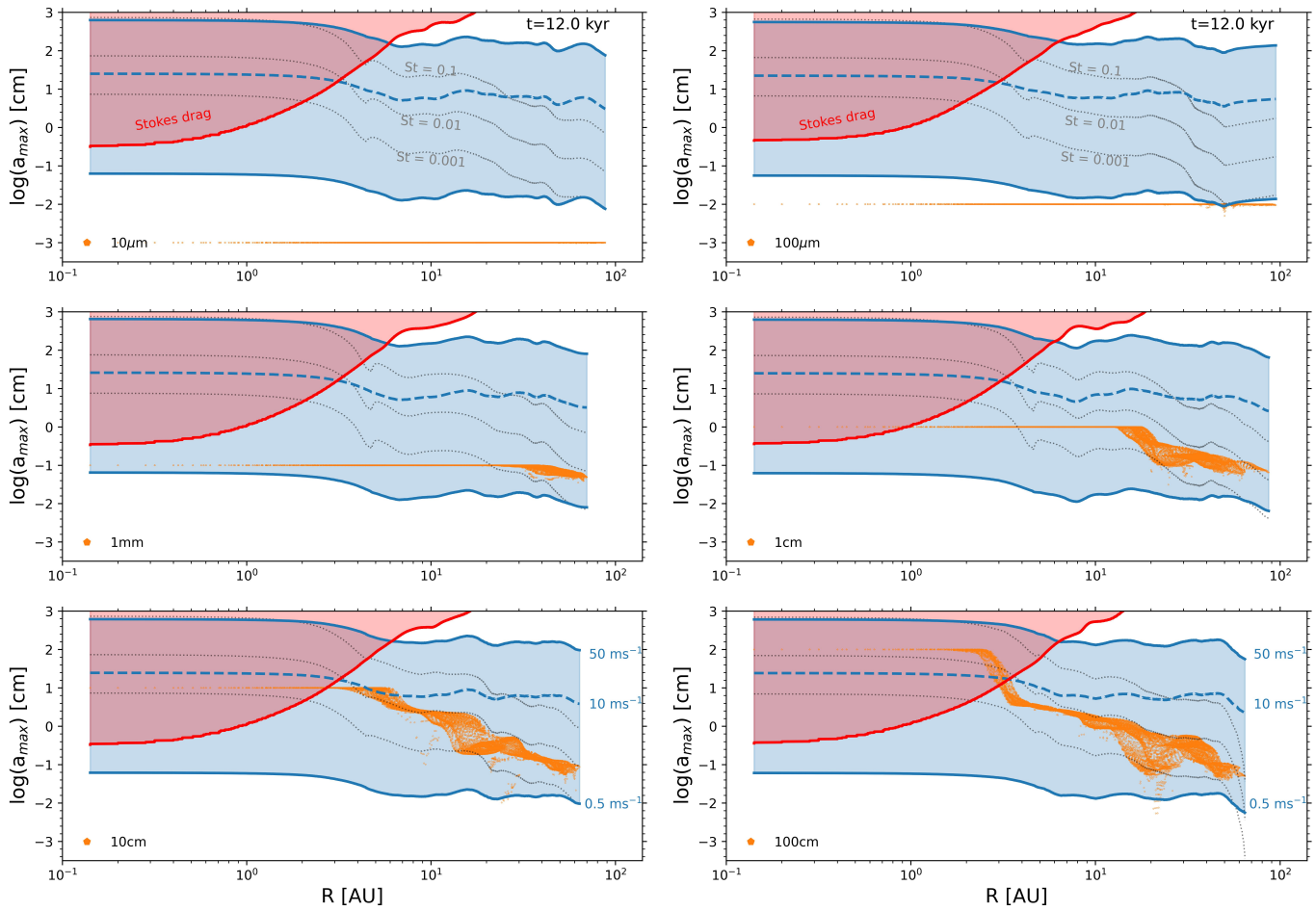


Fig. 3. Radial profiles of the maximum dust size $a_{\rm max}$ (orange symbols) for all six models with different maximum allowed size $a^{\rm cap}_{\rm max}$. The six panels (from left to right and from top to bottom) show the models with: $a^{\rm cap}_{\rm max}$=10 μm, $a^{\rm cap}_{\rm max}$=100 μm, $a^{\rm cap}_{\rm max}$=1.0 mm, $a^{\rm cap}_{\rm max}$=1.0 cm, $a^{\rm cap}_{\rm max}$=10 cm, and $a^{\rm cap}_{\rm max}$=100 cm. The blue curves indicate the maximum dust sizes in the fragmentation limited dust growth regime with the fragmentation velocities from 0.5 m s^{-1} (lower solid curve) through 10 m s^{-1} (middle dashed curve) and to 50 m s^{-1} (upper solid curve). The black dotted curves illustrate the dust sizes for a fixed Stokes number of 0.1, 0.01, and 0.001 (from top to bottom). The red curve separates the Stokes drag regime from that of Epstein drag.

ity outbursts (Liu et al. 2021; Houge et al. 2024) and this can assist planet formation in terrestrial zones. This finding is also interesting from the point of view of the pebble accretion scenario for planetary core growth (Johansen & Lambrechts 2017).

Figure 3 also indicates that $a_{\rm max}$ is characterized by a clear negative radial gradient if $a^{\rm cap}_{\rm max}$ is sufficiently large. Radial dust size gradients were inferred in protoplanetary disks at later stages of disk evolution by analyzing the radial distribution of dust spectral indices (e.g., Pinte et al. 2016; Tazzari et al. 2016). Our modeling demonstrates that the radial differentiation in the maximum dust size can exist already in the pre-stellar disks, provided that fragmentation and bouncing are inefficient at limiting dust growth.

Furthermore, disk models that study the dynamics of dust populations with a fixed dust size may only be justified if the dust growth barriers are efficient at holding the maximum dust size below 100 μm. Otherwise, the assumption of a constant dust size would not correctly reflect the actual radial distribution of dust size in the disk. In other words, dust grains with a size of 1.0 mm or 1.0 cm may not simply exist throughout the entire extent of the disk, and the choice of a population of dust grains with a fixed size at these large values may be not justified for the entire disk extent.

Interestingly, the radial distribution of the Stokes number St($a_{\rm max}$) corresponding to the maximum dust size $a_{\rm max}$ shows a different trend. We calculate St($a_{\rm max}$) in the disk midplane and depict them in Figure 4 for all six models with different $a^{\rm cap}_{\rm max}$. A positive radial gradient in St($a_{\rm max}$) is evident for $a^{\rm cap}_{\rm max} \leq$ 1.0 mm across most of the disk extent, except for the FCH where the trend reverses. For $a^{\rm cap}_{\rm max} \geq$ 10 cm, the radial distribution of St($a_{\rm max}$) exhibits no clear radial trend across the disk and is rather characterized by an order of magnitude scatter at a given radial distance, as was already noted when analyzing Figure 3. We remind the reader that these are the models in which dust growth is least restricted by the fragmentation and/or bouncing barriers and using the fixed Stokes number models may be justified in this case. Numerical models that compute the dynamics of multiple dust bins of fixed size or Stokes number without dust growth may use insights from our work for the multi-dust-bin approach (e.g. Rice et al. 2004; Lebreuilly et al. 2020). The case where all disk volume is considered, and not only the disk midplane as above, is further studied in Appendix B. We note that the negative

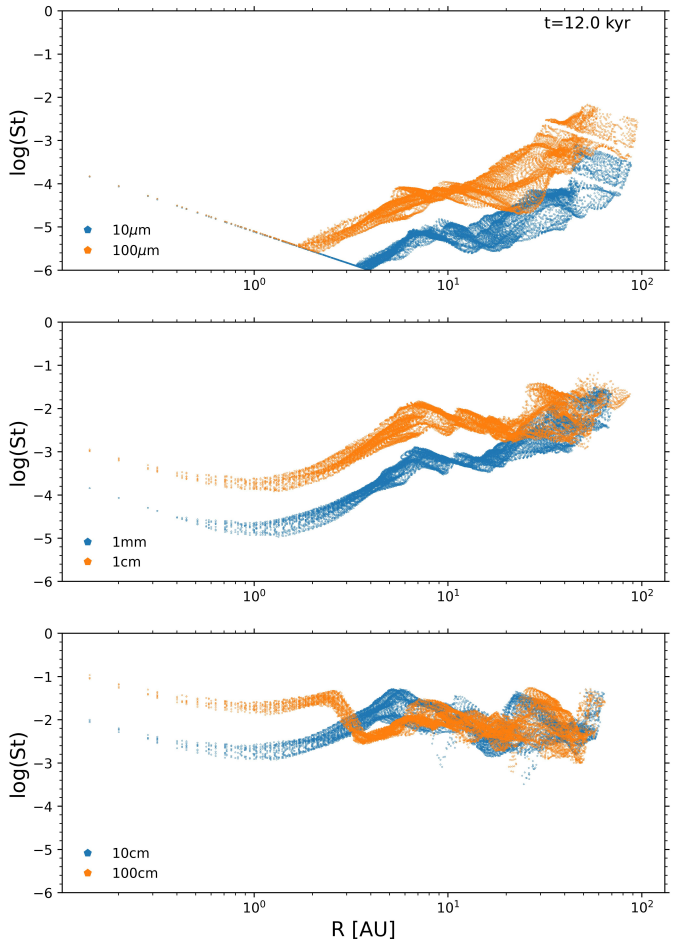


Fig. 4. Similar to Fig. 2 but for the Stokes number that corresponds to $a_{\rm max}$.

gradient of St at $R < 4$ au in the $a_{\rm max}^{\rm cap} \leq 100$ μm models is caused by setting a lower limit on the stopping time in our simulations and is thus an artificial feature.

Another interesting conclusion that can be drawn from Figure 4 is that the Stokes number hardly exceeds 0.1 in the early disk evolution, even in the model with $a_{\rm max}^{\rm cap} = 100$ cm. As described in our previous work (Vorobyov et al. 2024), this can partly be attributed to high gas densities and temperatures in young disks, both acting to reduce the stopping time of dust grains. The radial drift of dust can also contribute to limiting the Stokes number, especially in models with large $a_{\rm max}^{\rm cap} \geq 10$ cm. As dust particles grow in size and their Stokes number increases, they start drifting towards pressure maxima. An ensuing increase in gas temperature and density compensates an increase due to $a_{\rm max}$ in the definition of the Stokes number. This self-regulatory effect may also explain why strong radial gradients of the Stokes number diminish in models with increasing $a_{\rm max}^{\rm cap}$. The nonexistence of St $\gg 0.1$ in young disks, at least in the disk midplane, should be taken in consideration when studying the dust enrichment in spiral arms as regions of local pressure maxima (Rice et al. 2004; Boss et al. 2020; Rowther et al. 2024). Low St may hinder this process until, possibly, a much later stage of disk evolution when disk density and temperature drop and St may begin to approach unity.

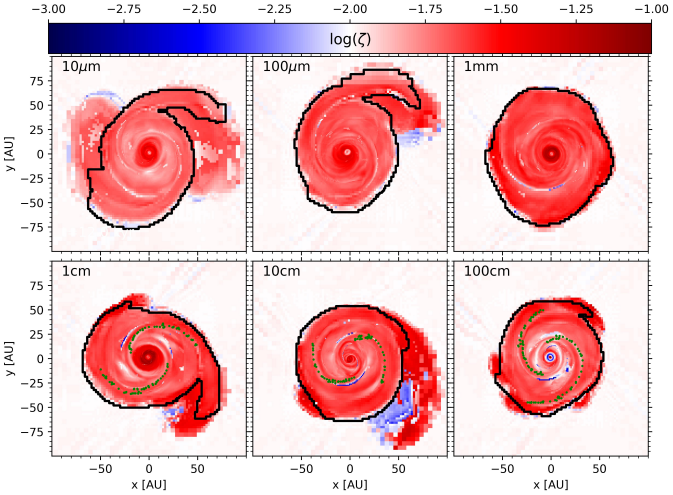


Fig. 5. Ratio of the total dust to gas volume densities in the disk midplane, ζ, at $t = 12$ kyr asfter disk formation. Six models with the maximum allowed dust size $a_{\rm max}^{\rm cap}$ are shown from left to right and from top to bottom: 10 μm, 100 μm, 1.0 mm, 1.0 cm, 10 cm, and 100 cm. The black contour curves delineate the disk extent. The green circles mark the position of the spiral arms in the latter three models.

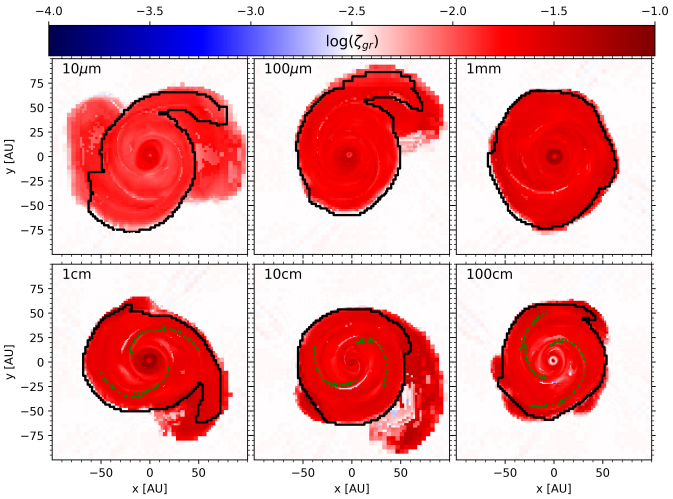


Fig. 6. Similar to Fig. 5 but for the ratio of the grown dust to gas volume densities, $\zeta_{\rm gr}$.

Finally, we note a steep change in $a_{\rm max}$ and St in the $a_{\rm max}^{\rm cap} \geq 100$ cm at around 3 au. This feature is likely caused by efficient radial dust drift towards the pressure-supported FHSC, which results in a local minimum in the dust-to-gas mass ratio at this radial distance, see Figure 10 below. This also makes dust growth in this regions strongly drift-dominated.

3.3. Dust enhancement

Figures 5 and 6 present the dust-to-gas mass ratios in the disk midplane at the end of our simulations ($t = 12$ kyr after disk formation). In particular, Figure 5 shows $\zeta_{\rm gr} = \rho_{\rm d,gr}/\rho_{\rm g}$, namely, the ratio of the grown dust density to that of gas, while Figure 6 displays $\zeta = (\rho_{\rm d,gr} + \rho_{\rm d,sm})/\rho_{\rm g}$, which is the ratio of the total dust density to that of gas. We note that the initial adopted values of ζ and $\zeta_{\rm gr}$ at the onset

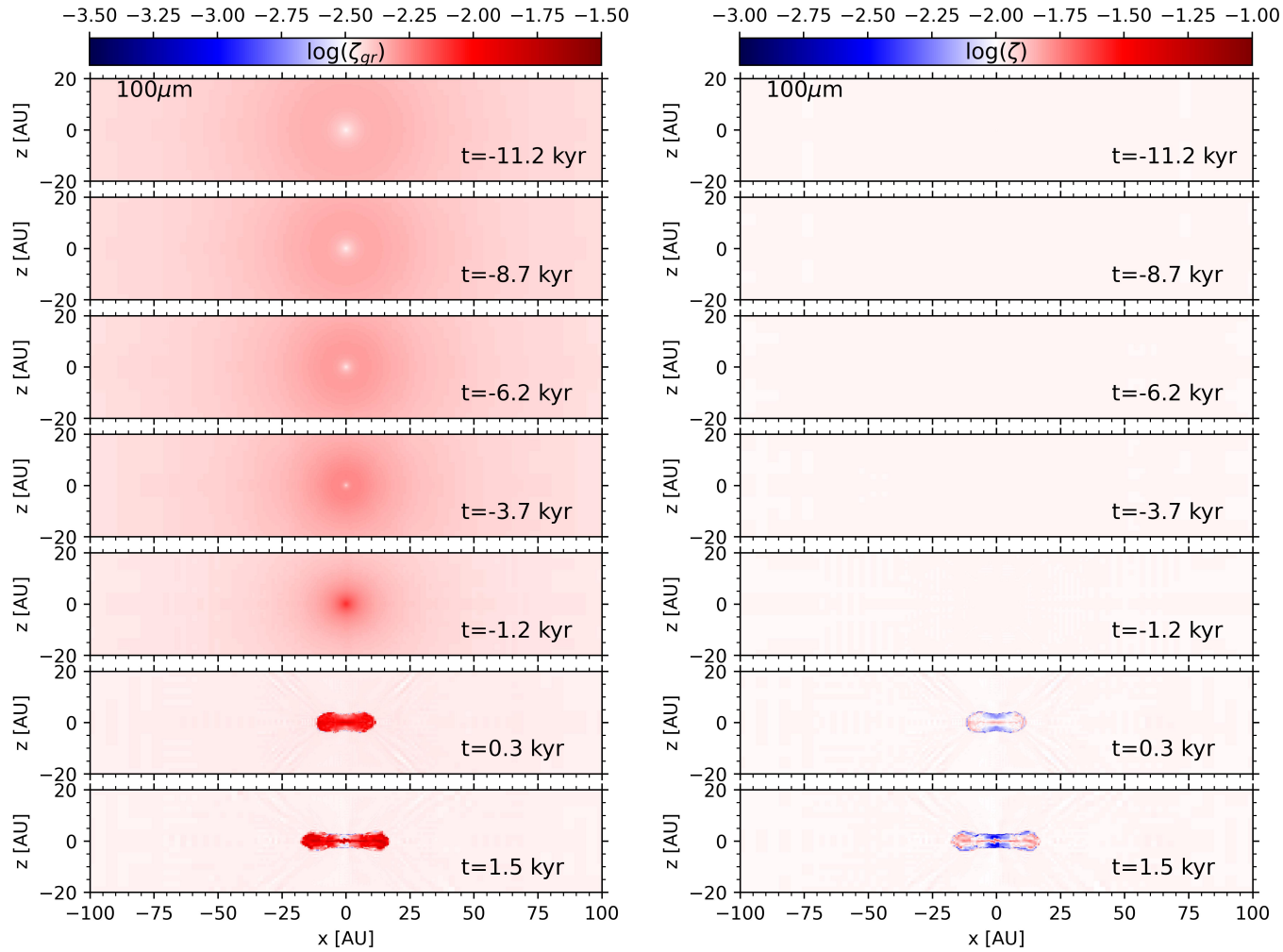


Fig. 7. Time evolution of $\zeta_{\rm gr}$ and ζ in the $x-z$ slice for the $a_{\rm max}^{\rm cap} = 100$ μm model. Left- and right-hand side group of panels represent the grown dust-to-gas mass ratio $\zeta_{\rm gr}$ and the total dust-to-gas mass ratio ζ, respectively. Note that the white color is reserved for the initial values of $\log\zeta_{\rm gr} = -2.51$, while the shades of red correspond to dust enhancements. Time is counted from the disk formation instance, which is 193 kyr after the onset of simulations.

of the prestellar cloud core collapse are $\log\zeta = -2.0$ and $\log\zeta_{\rm gr} = -2.51$.

Clearly, all models show dust enhancements in the disk midplane throughout most of the disk extent outlined by the black contour curves as determined by the disk tracking algorithm (see Sect. 2.6). The magnitude of this effect is stronger for models with a larger allowed dust size, but even the models with the lowest $a_{\rm max}^{\rm cap} = 10$ μm and $a_{\rm max}^{\rm cap} = 100$ μm show notable dust enhancements in the disk midplane. Dust enhancement in these latter models may be due to a particular arrangement of Stokes numbers that increase both with radial distance and distance from the disk midplane, see Figures 4 and B.1. This can cause a traffic jam effect in the disk as dust particles at smaller distances drift slower. However, low values of the Stokes number in the disk midplane should reduce the efficiency of this effect as far as the radial dust drift is concerned. Vertical settling, however, may play an important role in dust enhancement, as we later demonstrate in Sect. 3.4.

A closer look at the regions just outside the disk can hint at another possible explanation for the observed dust enhancement. These regions are characterized by the values of ζ and $\zeta_{\rm gr}$ that are slightly higher than their counterparts at the onset of cloud core collapse ($\log\zeta = -1.98$ against the initial $\log\zeta = \mathbf{-2.0}$ and $\log\zeta_{\rm gr} = -2.49$ against the initial $\log\zeta_{\rm gr} = -2.51$), suggesting that some dust enhancement may have taken place already in the predisk collapse stage.

To test this hypothesis, we plotted in the left column of Figure 7 the ratios $\zeta_{\rm gr}$ for the $a_{\rm max}^{\rm cap} = 100$ μm model in the evolution stage immediately preceding the disk formation instance. For this case, the vertical slices through the $x-z$ plane at $y = 0$ are shown. The time is counted from the disk formation instance and for this chosen timeline the negative time corresponds to the predisk stage. We see that at $t = -11.2$ kyr, well before the disk formation instance, the inner regions of the collapsing core are already enhanced in grown dust above the initial values of $\log\zeta_{\rm gr} = -2.51$. At $t = -1.2$ kyr, the maximum grown dust enhancement in the center of the collapsing core reaches $\log\zeta_{\rm gr} = -2.09$ in the $a_{\rm max}^{\rm cap} = 100$ μm model. When the disk begins to form, it already carries the gene of this early enrichment phase in grown dust, as can be seen in the bottom panels of Fig. 7. The maximum grown dust enrichment there is $\log\zeta_{\rm gr} = -1.79$. Efficient settling to the disk midplane is also observed in this model.

As the right column in Figure 7 demonstrates, dust enhancement in the predisk stage turns out to be much smaller when the total dust-to-gas ratio ζ (rather than $\zeta_{\rm gr}$) is considered. In particular, in the $a_{\rm max}^{\rm cap} = 100$ μm model the maximum value just before the disk formation instance is $\log\zeta = -1.98$, and this is only a minor increase when compared to the initial value of $\log\zeta = -2.0$ at the onset of collapse. Only after the disk has formed, notable enhancements in ζ near the disk midplane start to occur. This implies that dust growth followed by the conversion of small to grown dust (the S-term in Eqs. 4 and 5), is mainly responsible for the enhancement in grown dust ($\zeta_{\rm gr}$) in the predisk stage. Dust drift in this stage plays only a minor role.

We confirmed this conjecture by analyzing the radial distributions of $a_{\rm max}$, $\zeta_{\rm g}$, $\zeta - \zeta_{\rm gr}$ (i.e., the small dust to gas mass ratio), and the dust growth timescale during the predisk stage of cloud collapse, shown in Figure 8 for the $a_{\rm max}^{\rm cap} = 10$ μm model at 3.7 kyr before the disk formation instance. The gas density in the center of the collapsing cloud has increased by a factor of 500 compared to the initial distribution. Dust growth predominantly occurs in this inner region because the Stokes number reaches (and surpasses) unity there, see also Figure C.1 in Appendix C. The dust growth timescale calculated as $t_{\rm dust.growth} = a_{\rm max}/\mathcal{D}$ is about 10 kyr and is much shorter than the collapse timescale, $t_{\rm collapse} = 193$ kyr. We note, however, that the Stokes number is normalized to the Keplerian frequency $\Omega_{\rm K}$ in the growth rate term, which is relevant for circumstellar disks where the turnover frequency of the largest turbulent eddy is usually assumed to be equal the epicyclic frequency due to the Coriolis force, and namely $\Omega_{\rm K}$ for Keplerian disks (Ormel & Cuzzi 2007). In the envelope, the eddy turnover frequency may be different and this case is considered in more detail in Appendix D.

.

Figures 7–8 demonstrate that dust growth and conversion of small to grown dust are responsible for the predisk enhancement in grown dust. Differential collapse of gas and dust in the envelope seems to play only a minor role. We can further estimate the extent to which dust motion in the envelope is decoupled from that of gas considering the following arguments. Let us consider the initial stages of prestellar cloud collapse. Figure 9 presents the stopping time of grown dust in the envelope calculated at the onset of collapse. Its value ranges from < 1.0 kyr in the inner plateau to ≈ 10 kyr at the cloud outer edge. We remind the reader that the time from the onset of collapse to the FHSC formation instance is about 193 yr, most of which is consumed by slow cloud contraction. This means that the predisk phase of the gravitationally contracting cloud is much longer than the stopping time, implying that the infalling grown dust quickly attains an equilibrium with the slowly contracting gas via the mutual friction force.

This state of equilibrium can be described by the relative velocity of grown dust to gas as (Birnstiel 2024)

$$\boldsymbol{u} - \boldsymbol{v} = \frac{t_{\rm stop}}{\rho_{\rm g}(1+\zeta_{\rm gr})}\boldsymbol{\nabla} P. \quad (15)$$

We note that the gravity force cancels out in this equation. We can further calculate the drift timescale of the grown dust while it contracts together with the gas as $t_{\rm drift} = R/|\boldsymbol{u} - \boldsymbol{v}|$, where R is the radial distance from the center of the cloud. The corresponding values are plotted in Figure 9 and are a factor of several longer than the collapse timescale. This suggests that dust enrichment due to drift in the predisk stage is insignificant, which is confirmed by examining the total dust-to-gas ratios in the right panel of Figure 7.

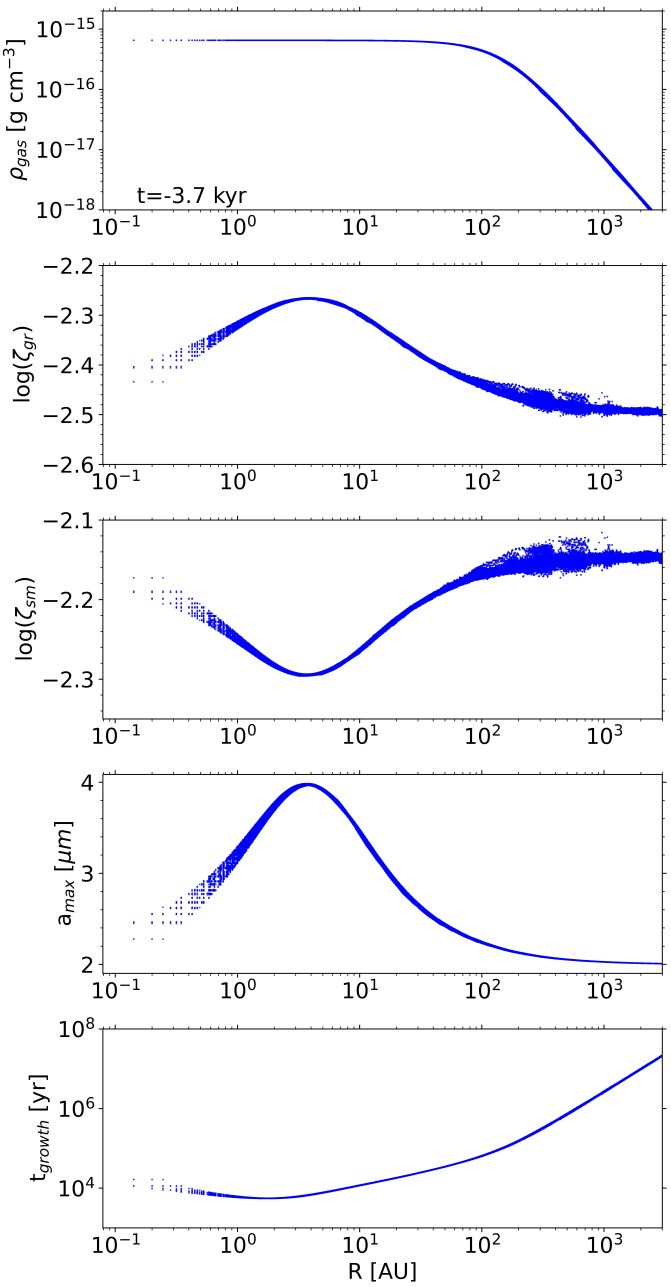


Fig. 8. Radial profiles of the characteristics of the collapsing cloud in the $a_{\rm max}^{\rm cap} = 10$ μm at 3.7 kyr before the disk formation instance. Shown are (from top to bottom): the gas volume density, grown dust to gas mass ratio, small dust to gas mass ratio, maximum dust size, and the dust growth timescale.

Finally, the position of the spiral arms as the local peaks in the midplane gas density are shown for three models with largest allowed dust sizes are plotted in Figures 5 and 6. Dust enhancements do not clearly correlate with the position of spiral arms. Several previous studies reported the correlation (Rice et al. 2004; Boss et al. 2020; Rowther et al. 2024) and this disagreement can be understood if we com-

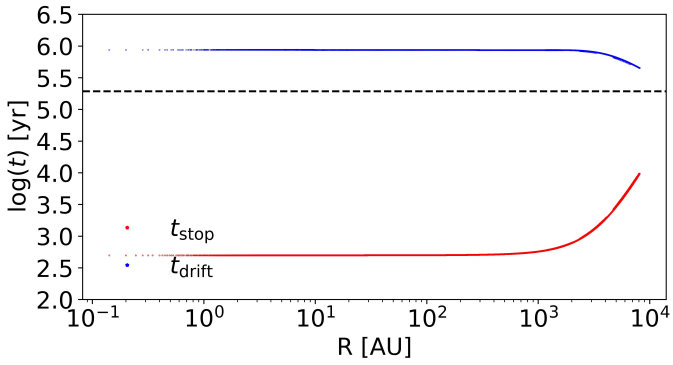


Fig. 9. Characteristic dust drift time and stopping time, t_{drift} and t_{stop}, as a function of radial distance from the cloud core center. Both values are calculated at the onset of cloud core collapse. The horizontal dashed line marks the time instance when the FHSC forms.

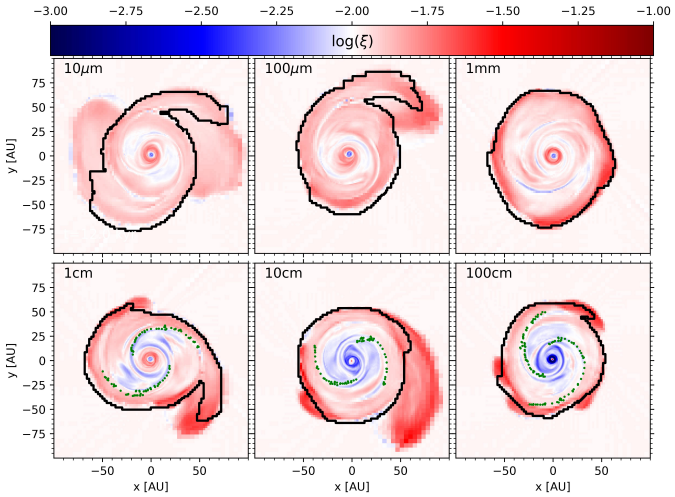


Fig. 10. Similar to Fig. 5 but for the ratio of the total dust to gas surface densities ξ.

pare the considered dust sizes and, in particular, the Stokes numbers. In aforementioned studies, dust efficiently concentrates in spiral arms if its Stokes number is around unity. However, such large Stokes numbers are hardly achievable in the earliest stages of disk formation. As described in Vorobyov et al. (2024), the disk in this stage is warmer and denser than its class II counterpart and the corresponding St hardly exceeds 0.1 (see Fig. 4). The agile and nonsteady nature of the spiral pattern in this early evolution stage, see Figure 1, may also work against clear dust concentration towards spiral arms.

3.4. Ratios of dust-to-gas surface densities

In the previous section, we considered dust enhancement in the midplane of the disk. However, it is also worth considering the dust-to-gas mass ratios derived from the vertically integrated dust and gas volume densities, because the dust density in the disk midplane depends on yet to be constrained disk turbulence (Rosotti 2023). The resulting ratios $\xi = (\Sigma_{d,gr} + \Sigma_{d,sm})/\Sigma_g$ are plotted in Figure 10 for all six models at $t = 12$ kyr. The values of the surface densities of gas (Σ_g), grown dust ($\Sigma_{d,gr}$), and small dust ($\Sigma_{d,sm}$) were calculated by vertically integrating the corresponding volume densities in the $100 \times 100 \times 100$ au cube centered on the coordinate center and encompassing the entire disk.

The ratio ξ is highly nonhomogeneous across the disk extent. Local enhancements in dust are alternated with local depletions. The variations in ξ around the initial value of 0.01 become stronger for higher a_{max}^{cap} models. We checked the total masses of dust (both small and grown) and gas in the $100 \times 100 \times 100$ au cube at $t = 12$ kyr, and the resulting ratio of integrated dust to gas masses is about 0.0104. This quite small positive deviation from the initial value of 0.01 is consistent with the earlier established minor role of differential collapse of gas and dust in creating dust enhancements. Local processes in the disk should be responsible for substantial local variations in ξ seen in Figure 10, such as radially varying efficiency of vertical dust settling and local perturbations by spiral density waves. Further focused simulations are needed to better understand the reason.

4. Caveats

Here, we discuss several model limitations that may, in principal, affect dust enrichment and growth in the early stages of disk formation. We start our simulations from the gravitational collapse of the Bonnor-Ebert sphere. If the initial conditions were rather those of a homogeneous sphere, then the collapse time might have been shorter and the predisk dust enrichment may be weaker. Magnetic fields may also change the character of cloud core collapse, thus affecting the initial dust enrichment (Machida & Basu 2020; Vallucci-Goy et al. 2024). The process of protostar formation during the second collapse of the FHSC has not been considered and may lead to a subtle interplay between the disk forming around the protostar and that formed around the FHSC (Tomida et al. 2015), which may affect the dust dynamics and growth efficiency. Finally, considering dust growth in the collapsing envelope requires a different approach from that employed to model this process in the disk (Silsbee et al. 2022). All these issues deserve further investigation.

5. Conclusions

In this work, we studied the initial stages of disk formation and evolution using the three-dimensional numerical hydrodynamics simulations in the polytropic limit. The gas and dust dynamics were computed from the onset of the cloud core collapse to 12 kyr after the FHSC formation. The simulations were terminated just before the collapse of the FHSC and formation of the protostar.

Unlike our previous study (Vorobyov et al. 2024), where dust growth was halted at the fragmentation barrier corresponding to $v_{frag} = 5.0$ m s^{-1}, here we adopted a range of v_{frag} from 0.5 to 50 m s^{-1} as suggested by various laboratory experiments, and also considered the effects of electrostatic and bouncing barriers. This is implicitly done by setting several upper limits on the dust size a_{max}^{cap} to which dust can grow, ranging from 10 μm to 100 cm, with a multiple of ten. The lowest value of a_{max}^{cap} can be viewed as that imposed by the electrostatic barrier, while the other higher values of a_{max}^{cap} correspond to various fragmentation (as defined by v_{frag}) and bouncing barriers. The drift barrier to dust growth is accounted for self-consistently via the solution of the dust dynamics equation. Our findings can be summarized as follows.

- Dust growth starts already in the collapse stage. Both the FHSC and the disk begin to form in an environment that is already enriched in grown dust compared to the maximum dust size in the initial cloud core. Differential collapse of gas and dust in the cloud has only minor effect on dust enrichment at the onset of disk formation.
- The efficiency of dust growth in the disk formation stage is limited by dust growth barriers. If the maximum size of dust grains in a young protoplanetary disk is below 100 μm, then dust growth is likely limited by the bouncing or electrostatic barriers. For larger dust grains, the collisional fragmentation and drift are the main dust growth barriers.
- The disk midplane becomes quickly enriched with dust owing to efficient dust settling. On the other hand, the vertically integrated distribution of dust shows notable local deviations around the canonical 1:100 dust-to-gas mass ratio, whereas the globally integrated value deviates negligibly from the initial 1:100 value. Local hydrodynamic flows in a gravitationally unstable disk may be responsible for these local variations but the exact reason is to be determined.
- In the fragmentation- and drift-limited regimes, the maximum dust size exhibits a profound negative radial gradient throughout most of the disk extend in the very early stages of evolution. A constant-dust-size approximation may not be appropriate in this case.
- When choosing between the constant-size or constant-St approximations, the latter is preferable, particularly, for disk conditions where dust can grow above 10 cm in size.

Acknowledgements. We are grateful to the referee for an insightful review, which helped us to reconsider our initial conclusions and to improve the manuscript. This work was supported by the FWF project I4311-N27 (E. I. V.) and RFBR project 19-51-14002 (A. S.). Simulations were performed on the Vienna Scientific Cluster (VSC)[1] and on the Narval Cluster provided by Calcul Québec[2] and the Digital Research Alliance of Canada[3].

References

Ahmad, A., González, M., Hennebelle, P., & Commerçon, B. 2023, A&A, 680, A23
Akimkin, V., Ivlev, A. V., Caselli, P., Gong, M., & Silsbee, K. 2023a, ApJ, 953, 72
Akimkin, V., Ivlev, A. V., Caselli, P., Gong, M., & Silsbee, K. 2023b, ApJ, 953, 72
Akimkin, V. V. 2015, Astronomy Reports, 59, 747
Akimkin, V. V., Ivlev, A. V., & Caselli, P. 2020, ApJ, 889, 64
ALMA Partnership, Brogan, C. L., Pérez, L. M., et al. 2015, ApJ, 808, L3
Bate, M. R. 2022, MNRAS, 514, 2145
Bhandare, A., Kuiper, R., Henning, T., et al. 2020, A&A, 638, A86
Bhandare, A., Kuiper, R., Henning, T., et al. 2018, A&A, 618, A95
Binney, J., Tremaine, S., & Ostriker, J. 1987, Galactic Dynamics, Princeton series in astrophysics (Princeton University Press)
Birnstiel, T. 2024, ARA&A, 62, 157
Birnstiel, T., Fang, M., & Johansen, A. 2016, Space Sci. Rev., 205, 41
Birnstiel, T., Klahr, H., & Ercolano, B. 2012, A&A, 539, A148
Blum, J. 2018, Space Sci. Rev., 214, 52
Blum, J. & Wurm, G. 2008, ARA&A, 46, 21
Boss, A. P., Alexander, C. M. O., & Podolak, M. 2020, ApJ, 901, 81
Cridland, A. J., Rosotti, G. P., Tabone, B., et al. 2022, A&A, 662, A90
Drążkowska, J., Bitsch, B., Lambrechts, M., et al. 2023, in Astronomical Society of the Pacific Conference Series, Vol. 534, Protostars and Planets VII, ed. S. Inutsuka, Y. Aikawa, T. Muto, K. Tomida, & M. Tamura, 717
Galametz, M., Maury, A. J., Valdivia, V., et al. 2019, A&A, 632, A5
Gundlach, B. & Blum, J. 2015, ApJ, 798, 34
Hennebelle, P., Commerçon, B., Lee, Y.-N., & Charnoz, S. 2020, A&A, 635, A67
Houge, A., Macías, E., & Krijt, S. 2024, MNRAS, 527, 9668
Inutsuka, S.-i. 2012, Progress of Theoretical and Experimental Physics, 2012, 01A307
Johansen, A. & Lambrechts, M. 2017, Annual Review of Earth and Planetary Sciences, 45, 359
Joos, M., Hennebelle, P., & Ciardi, A. 2012, A&A, 543, A128
Koga, S. & Machida, M. N. 2023, MNRAS, 519, 3595
Kratter, K. M., Matzner, C. D., & Krumholz, M. R. 2008, ApJ, 681, 375
Laibe, G. & Price, D. J. 2014, MNRAS, 444, 1940
Larson, R. B. 1985, MNRAS, 214, 379
Lebreuilly, U., Commerçon, B., & Laibe, G. 2020, A&A, 641, A112
Lee, C.-F., Li, Z.-Y., & Turner, N. J. 2020, Nature Astronomy, 4, 142
Lin, M.-K. & Youdin, A. N. 2017, ApJ, 849, 129
Liu, H. B., Tsai, A.-L., Chen, W. P., et al. 2021, ApJ, 923, 270
Lorén-Aguilar, P. & Bate, M. R. 2015, MNRAS, 454, 4114
Machida, M. N. & Basu, S. 2020, MNRAS, 494, 827
Machida, M. N., Inutsuka, S.-i., & Matsumoto, T. 2014, MNRAS, 438, 2278
Machida, M. N. & Nakamura, T. 2015, MNRAS, 448, 1405
Marchand, P., Lebreuilly, U., Mac Low, M. M., & Guillet, V. 2023, A&A, 670, A61
Masunaga, H. & Inutsuka, S.-i. 2000a, ApJ, 531, 350
Masunaga, H. & Inutsuka, S.-i. 2000b, ApJ, 531, 350
Mathis, J. S., Rumpl, W., & Nordsieck, K. H. 1977, ApJ, 217, 425
McKevitt, J., Vorobyov, E. I., & Kulikov, I. 2024, J. of Parallel and Distributed Comp., 195, 104977
Molyarova, T., Vorobyov, E. I., Akimkin, V., et al. 2021, ApJ, 910, 153
Morbidelli, A., Marrocchi, Y., Ali Ahmad, A., et al. 2024, A&A, 691, A147
Okuzumi, S. 2009, ApJ, 698, 1122
Okuzumi, S., Momose, M., Sirono, S.-i., Kobayashi, H., & Tanaka, H. 2016, ApJ, 821, 82
Okuzumi, S., Tanaka, H., Takeuchi, T., & Sakagami, M.-a. 2011a, ApJ, 731, 95
Okuzumi, S., Tanaka, H., Takeuchi, T., & Sakagami, M.-a. 2011b, ApJ, 731, 95
Ormel, C. W. & Cuzzi, J. N. 2007, A&A, 466, 413
Pinte, C., Dent, W. R. F., Ménard, F., et al. 2016, ApJ, 816, 25
Rice, W. K. M., Lodato, G., Pringle, J. E., Armitage, P. J., & Bonnell, I. A. 2004, MNRAS, 355, 543
Rosotti, G. P. 2023, New A Rev., 96, 101674
Rowther, S., Nealon, R., Meru, F., et al. 2024, MNRAS, 528, 2490
Sai, J. I. C., Ohashi, N., Yen, H.-W., Maury, A. J., & Maret, S. 2023, ApJ, 944, 222
Sengupta, D., Cuzzi, J. N., Umurhan, O. M., & Lyra, W. 2024, ApJ, 966, 90
Silsbee, K., Akimkin, V., Ivlev, A. V., et al. 2022, ApJ, 940, 188
Steinpilz, T., Joeris, K., Jungmann, F., et al. 2020, Nature Physics, 16, 225
Stoyanovskaya, O. P., Vorobyov, E. I., & Snytnikov, V. N. 2018, Astronomy Reports, 62, 455
Tazzari, M., Testi, L., Ercolano, B., et al. 2016, A&A, 588, A53
Tomida, K., Machida, M. N., Saigo, K., Tomisaka, K., & Matsumoto, T. 2010, ApJ, 725, L239
Tomida, K., Okuzumi, S., & Machida, M. N. 2015, ApJ, 801, 117
Toro, E. 2019, Shock Waves, 29, 1065
Tsukamoto, Y., Machida, M. N., & Inutsuka, S.-i. 2021, ApJ, 920, L35
Tsukamoto, Y., Okuzumi, S., Iwasaki, K., Machida, M. N., & Inutsuka, S.-i. 2017, PASJ, 69, 95
Valdivia, V., Maury, A., Brauer, R., et al. 2019, MNRAS, 488, 4897
Vallucci-Goy, V., Lebreuilly, U., & Hennebelle, P. 2024, A&A, 690, A23
van der Marel, N., Dong, R., di Francesco, J., Williams, J. P., & Tobin, J. 2019, ApJ, 872, 112
Vorobyov, E. I., Akimkin, V., Stoyanovskaya, O., Pavlyuchenkov, Y., & Liu, H. B. 2018, A&A, 614, A98
Vorobyov, E. I. & Basu, S. 2005, ApJ, 633, L137
Vorobyov, E. I., Elbakyan, V. G., Johansen, A., et al. 2023a, A&A, 670, A81

[1] https://vsc.ac.at/
[2] https://www.calculquebec.ca/
[3] https://alliancecan.ca/

Vorobyov, E. I., Kulikov, I., Elbakyan, V. G., McKevitt, J., & Güdel, M. 2024, A&A, 683, A202
Vorobyov, E. I., McKevitt, J., Kulikov, I., & Elbakyan, V. 2023b, A&A, 671, A81
Vorobyov, E. I., Skliarevskii, A. M., Elbakyan, V. G., et al. 2019, A&A, 627, A154
Vorobyov, E. I., Skliarevskii, A. M., Molyarova, T., et al. 2022, A&A, 658, A191
Wada, K., Tanaka, H., Suyama, T., Kimura, H., & Yamamoto, T. 2009, ApJ, 702, 1490
Wada, K., Tanaka, H., Suyama, T., Kimura, H., & Yamamoto, T. 2011, ApJ, 737, 36
Ward-Thompson, D., Hartmann, L., & Nutter, D. J. 2005, MNRAS, 357, 687
Windmark, F., Birnstiel, T., Ormel, C. W., & Dullemond, C. P. 2012, A&A, 544, L16
Zsom, A., Ormel, C. W., Güttler, C., Blum, J., & Dullemond, C. P. 2010, A&A, 513, A57

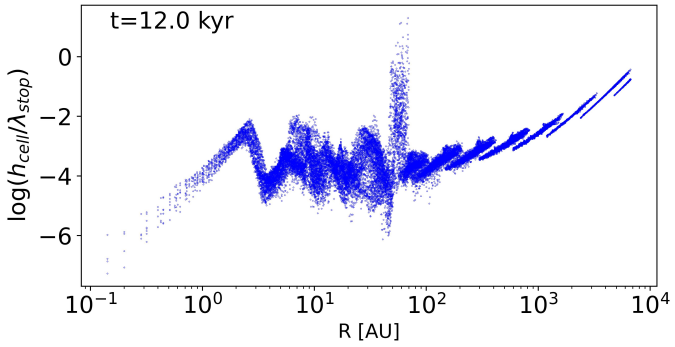


Fig. A.1. Ratio of the cell size to the stopping length as a function of distance from the coordinate center.

Appendix A: Dust as a fluid

It is not obvious that the dynamics of dust particles can be described using the gas hydrodynamics equations. One of the principle requirements is that the number of dust particles per computational cell is sufficiently large so that the mean dust densities and velocities obtained by integrating the corresponding distribution function of dust particles over the velocity space do not suffer from statistical noise. This is usually fulfilled with a large margin for typical spectrum of dust sizes in a protoplanetary disk (e.g., Vorobyov et al. 2022). Another requirement is that the stopping length, defined as $\lambda_{\rm stop} = |\boldsymbol{u}-\boldsymbol{v}|t_{\rm stop}$ should be shorter than the size of the cell, by analogy to the requirement on the mean free path of a gas molecule (or atom) in gas dynamics.

This latter requirement is checked in Figure A.1, which shows the ratio of the cell size to the stopping length as a function of distance from the coordinate center for model with $a_{\rm max}^{\rm cap} = 100$ cm at $t = 12$ kyr. This model is supposed to have the longest stopping time and, thus, the stopping length. The stopping length is much smaller than the size of the cell in the disk and in the collapsing envelope. However, there is one notable exception – the interface between the disk and the envelope around 70 au where the ratio can exceed unity. The reason can be seen in Figure A.2 showing the two-dimensional spatial maps of $t_{\rm stop}$ and $|\boldsymbol{u}-\boldsymbol{v}|$ in the disk midplane. Both quantities are higher at the disk-envelope interface than in the disk and in the inner envelope. The higher values of the relative velocity are likely caused by the shock, which forms where the infalling envelope meets the disk. The infalling gas is efficiently decelerated at the shock while the pressureless dust does it with a delay via the dust-to-gas friction. The stopping time is increased because dust experiences the first major episode of growth at the turbulent disk outer edge (see Fig. 3). In anyway, this peculiar region is narrow and transitory, and thus should not seriously affect our modeling.

Finally, we note that a purely pressureless fluid is subject to the development of delta shocks, which express themselves in an uncontrolled growth of density at discontinuities. It is an important property of the code to reproduce such a feature, as is done in Fig. C.9 of Vorobyov et al. (2024). However, these features also corrupt the flow of a pressureless fluid and the fluid approach becomes inapplicable. Fortunately, delta shocks do not form if a repulsion force other than pressure is present in the system, and this is the case in our models where the role of the repulsion

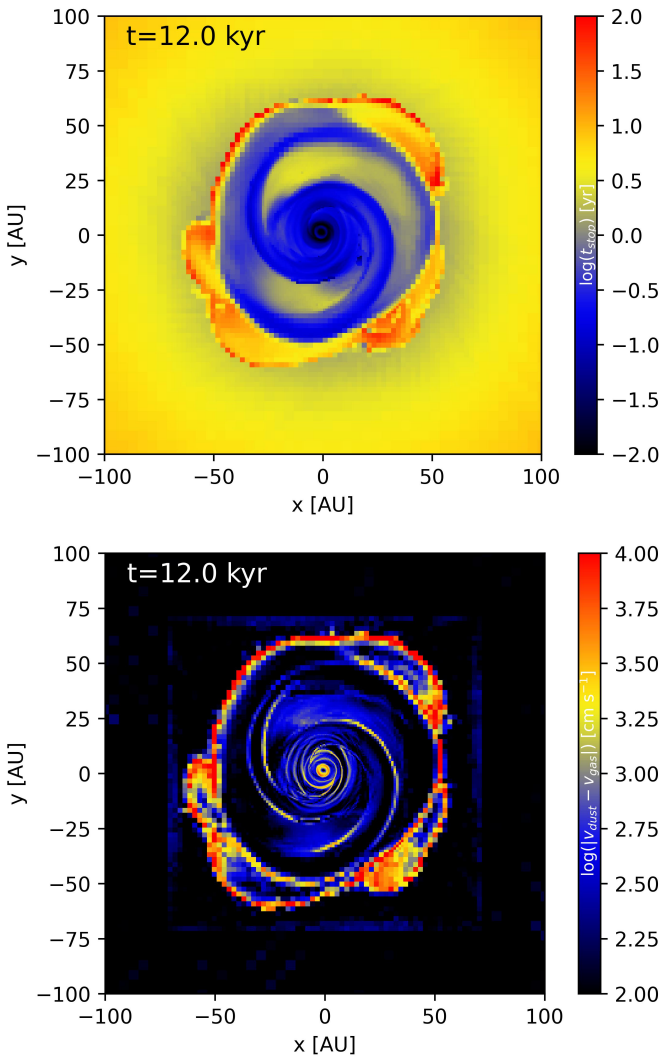


Fig. A.2. Stopping time (top panel) and the dust-minus-gas relative velocity by absolute value (bottom panel). The scale bars are in log yr and log cm s^{-1}.

force is played by the gas-to-dust friction (see, the $\boldsymbol{f}$-term in Eq. 6). As Fig. C.7 in Vorobyov et al. (2024) demonstrates, the dust flow becomes smooth, correctly reproducing the shock and discontinuity positions if dust to gas coupling is strong. This is the case for the disk where the Stokes number does not exceed 1.0 and is mostly below 0.1.

Appendix B: Maximum dust size and Stokes number throughout the vertical extent of the disk

Here, we briefly discuss the spatial distribution of the maximum dust size and Stokes number in the entire disk volume. Figure B.1 plots the corresponding values as a function of distance in the disk midplane for models with all six $a_{\rm max}^{\rm cap}$ considered. The blue dots represent the midplane values, while the red dots correspond to those in the rest of the disk vertical extent (hereafter, disk atmosphere). Dust grains of maximum size are found in the disk midplane and their maximum size decreases in the disk atmosphere. The lowest values of $a_{\rm max}$ are found near the disk-envelope interface, approaching those of the envelope, $a_{\rm max} = 2.0$ μm.

This distribution of dust grain size is expected for disks with vertical dust settling.

The Stokes number exhibits a more complicated trend. For models with $a_{\rm max}^{\rm cap} = 10$ μm and 100 μm, the spatial distribution of St is opposite to that of $a_{\rm max}$ – the lowest St are found in the disk midplane, while its values increase in the disk atmosphere. For models with $a_{\rm max}^{\rm cap} \geq 1.0$ cm, this anticorrelation diminishes and the disk atmosphere is mostly characterized by St that is generally lower than that in the disk midplane. Considering that the disk conditions (gas densities and temperatures) do not change notably from model to model (see Fig. 1), this difference in the Stokes number behavior can be attributed to efficient dust growth in the disk midplane. Although St may demonstrate an order of magnitude variations, models with a constant Stokes number are still preferable over those with a constant dust size when dust growth is allowed above 10 cm (e.g., models with $a_{\rm max}^{\rm cap}$=10 and 100 cm).

Appendix C: Stokes number in the infalling envelope of the predisk stage

Figure C.1 presents the Stokes number in the vertical $x-z$ cut through the $y = 0$ plane. The time period immediately preceding disk formation is shown. Clearly, the Stokes number is larger in the inner regions of the collapsing cloud, exceeding unity in its center. The bottom row shows a time instance right after the FHSC formation. The Stokes number decreases in this stage owing to a sharp increase in the gas volume density and temperature. We note that the Stokes number definition for the envelope may not be fully self-consistent, see the main text.

Appendix D: Dust growth rates in the envelope

Equation 10 defines the turbulence-induced collision velocities in disk conditions, which may deviate from those in the surrounding protostellar envelope. The original formulation from Ormel & Cuzzi (2007) requires specifying the velocity ($v_{\rm L}$) and spatial scales (L) of the largest turbulent eddy. In the α-prescription for disk turbulence, these scales are proportional to the local sound speed $c_{\rm s}$ and the gas vertical scale height $H_{\rm gas} = c_{\rm s}/\Omega_K$ (e.g., Sengupta et al. 2024):

$$v_{\rm L} = \sqrt{\alpha} c_{\rm s}, \quad \text{(D.1)}$$
$$L = \sqrt{\alpha} H_{\rm gas}. \quad \text{(D.2)}$$

The turbulence in the infalling envelope, if developed, may exhibit distinct properties compared to that in the disk. To quantify the influence of envelope turbulence on dust evolution, we compute the dust growth timescales employing the turbulence-induced velocity recipe from Ormel & Cuzzi (2007). We consider four parameter sets of $v_{\rm L}$ and L values, and assume the same physical structure of the collapsing cloud at 3.7 kyr as in Figure 8.

$$v_{\rm L} = 0.03 c_{\rm s}, \quad L = 0.5\,{\rm au}; \quad \text{(D.3)}$$
$$v_{\rm L} = 0.5 c_{\rm s}, \quad L = 100\,{\rm au}; \quad \text{(D.4)}$$
$$v_{\rm L} = 0.5 c_{\rm s}, \quad L = 1000\,{\rm au}; \quad \text{(D.5)}$$
$$v_{\rm L} = 1.0 c_{\rm s}, \quad L = 1000\,{\rm au}; \quad \text{(D.6)}$$
$$\quad \text{(D.7)}$$

The first case corresponds to the turbulence properties that are characteristic of the outer disk when it forms, while the next three cases explore the parameter space relevant for the envelopes (Ward-Thompson et al. 2005; Sai et al. 2023). Figure D.1 demonstrates the comparison between the dust growth timescale calculated based on a simplified recipe for disk conditions (Equation 10; blue line) and those for a stronger turbulence in the envelope. One can see that at the outer radii $R > 10 - 100$ au, the stronger turbulence in the envelope may lead to even faster growth rates than those shown in Figure 8. Thus, our key conclusion that dust growth starts in the contracting cloud in the evolution stage that precedes disk formation remains generally unchanged. We should note, however, that the value of $t_{\rm growth}$ is only an estimate as the dust growth rates depend on the grain size itself. More detailed modeling of the dust size evolution requires proper consideration of the turbulence changes at the envelope-disk interface, which deserves a separate study.

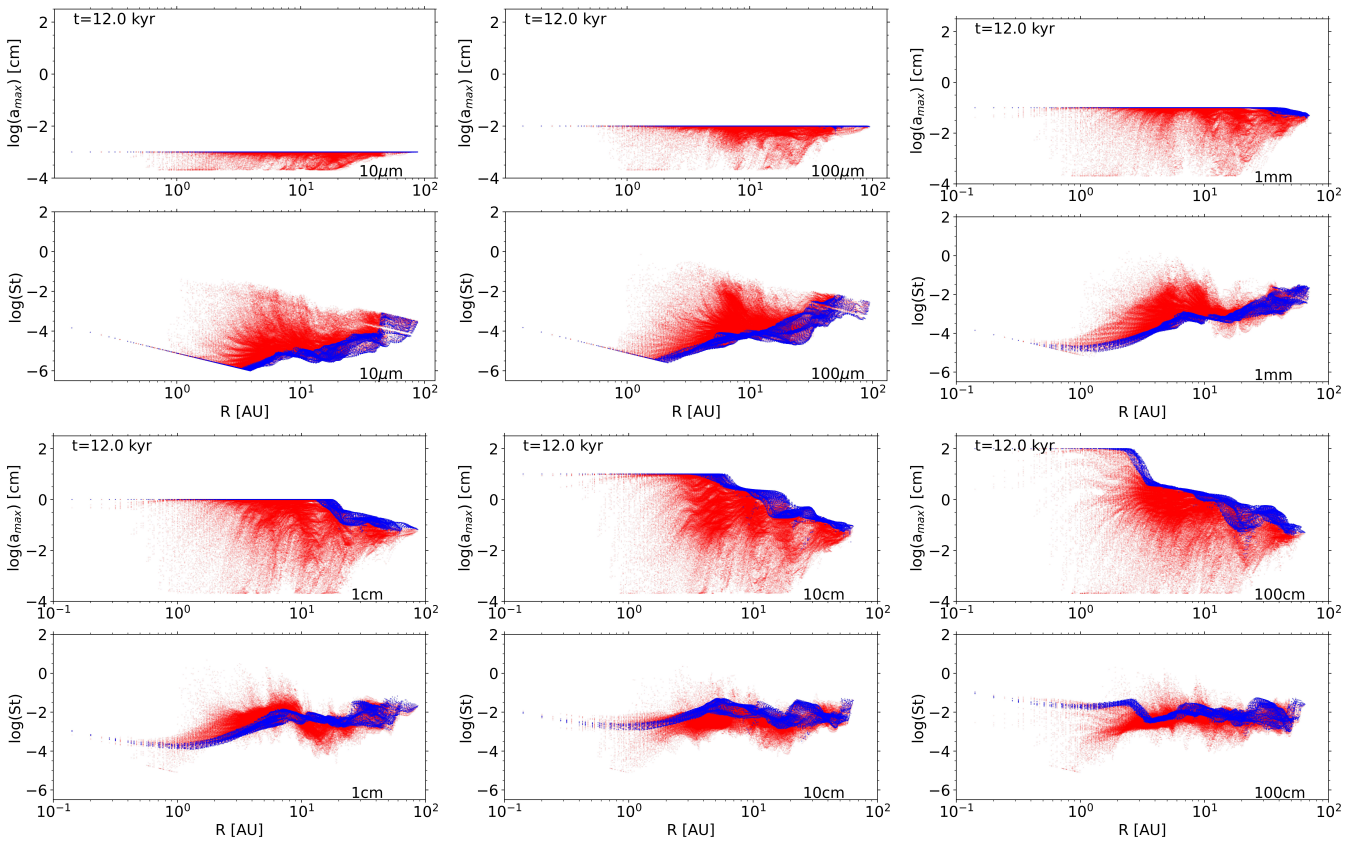


Fig. B.1. Dust maximum size and Stokes number in the disk midplane (blue dots) and disk atmosphere (red dots) as a function of distance in the disk midplane. The envelope is excluded. Two pairs of rows show, from left to right, the models with $a_{\rm max}^{\rm cap}$=10 μm, 100 μm, 1.0 mm, 1.0 cm, 10 cm, and 100 cm.

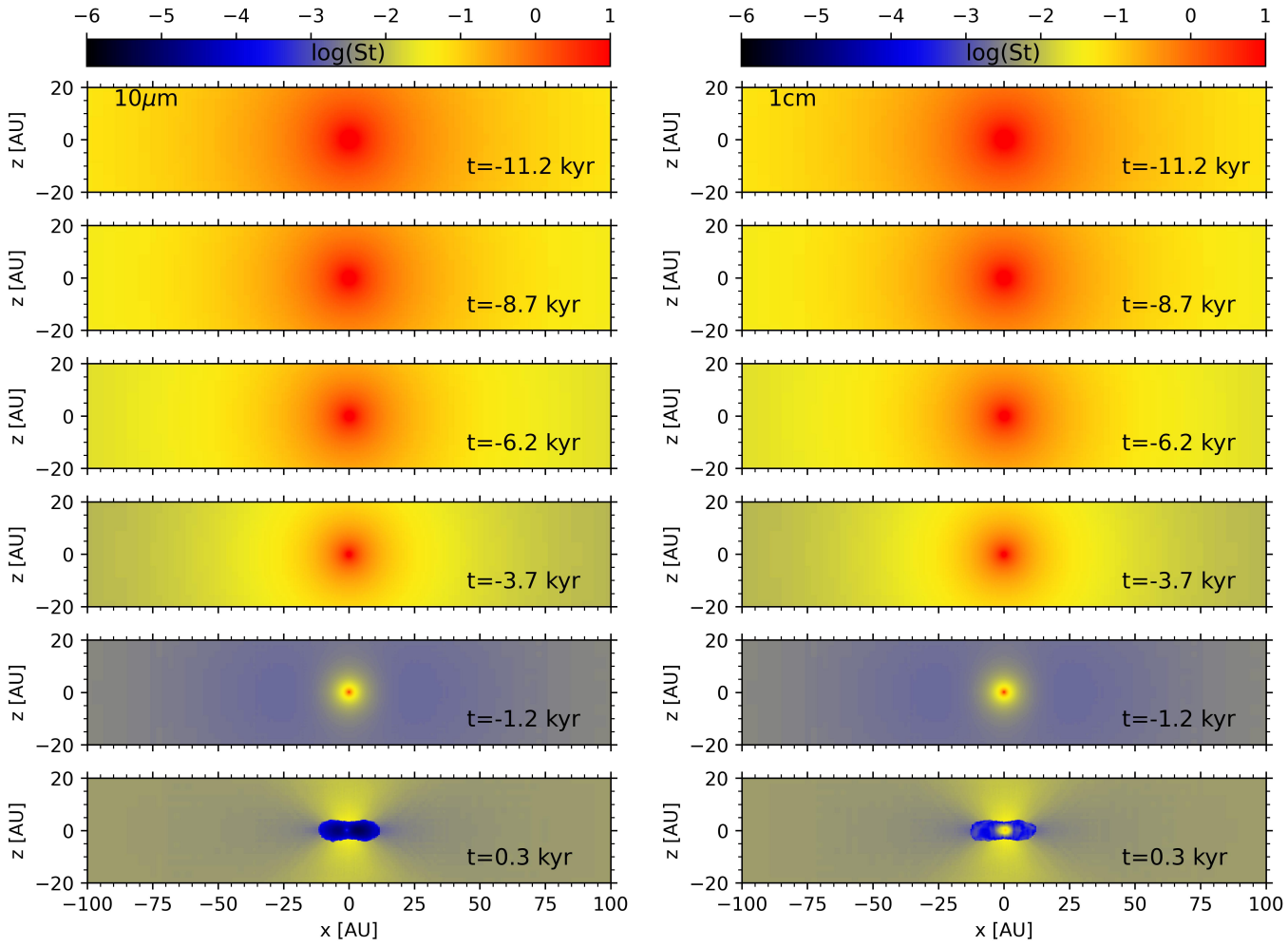


Fig. C.1. Time evolution of St in the $x-z$ slice. Left- and right-hand side group of panels belong to the models with $a_{\rm max}^{\rm cap} = 10$ μm and $a_{\rm max}^{\rm cap} = 1.0$ cm, respectively. Time is counted from the disk formation instance

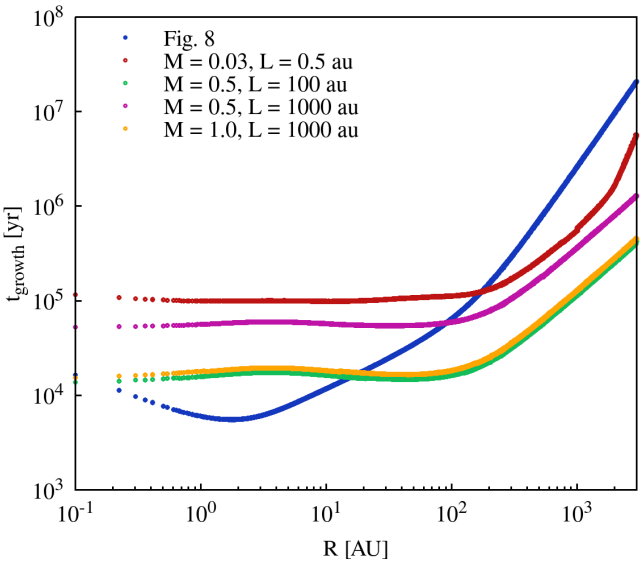


Fig. D.1. Dust growth timescales in the collapsing cloud for different turbulence properties in the envelope, parametrized by the Mach number $M = v_{\rm L}/c_{\rm s}$ and the spatial scale L of the largest turbulent eddy.